

**Computational Methodology for Aeroacoustic Simulation
Using Immersed Boundaries and Complex Geometry**

by

Eric Brown-Dymkoski

B.S., Mechanical Engineering, Washington State University, 2008

A thesis submitted to the
Faculty of the Graduate School of the
University of Colorado in partial fulfillment
of the requirements for the degree of
Masters of Science
Department of Mechanical Engineering

2012

This thesis entitled:
Computational Methodology for Aeroacoustic Simulation Using Immersed Boundaries and
Complex Geometry
written by Eric Brown-Dymkoski
has been approved for the Department of Mechanical Engineering

Oleg V. Vasilyev

Prof. Daven Henze

Prof. Kenneth Jansen

Date _____

The final copy of this thesis has been examined by the signatories, and we find that both the content and the form meet acceptable presentation standards of scholarly work in the above mentioned discipline.

Brown-Dymkoski, Eric (M.S., Mechanical Engineering)

Computational Methodology for Aeroacoustic Simulation Using Immersed Boundaries and Complex Geometry

Thesis directed by Prof. Oleg V. Vasilyev

The problem of computational aeroacoustic modelling is complex and of practical interest, especially for external flows around arbitrary geometries. Aeroacoustic interactions are of a higher order than aerodynamics, and as such, particular care must be taken in the modelling.

For efficiency, an adaptive multi-resolution grid is used to reduce the number of grid points while still resolving pertinent scales. The compressible Navier-Stokes equations are solved using the Adaptive Wavelet Collocation Method (AWCM), where wavelet decomposition provides a fast and efficient method for grid compression while maintaining rigorous control over the error.

The primary focus of this thesis is developing methodologies for efficient handling of solid obstacles within flows. Proper modelling of the effects of arbitrarily shaped obstacles is a prominent issue for fluid modelling, for which there are several approaches. Immersed boundary methods are well suited for use with rectilinear grid, such as that of AWCM, as they circumvent the need for a body-conformal mesh. The geometry can be efficiently generated through external CAD software, and ray-tracing algorithms used to create accurate masking functions. Ray-tracing is attractive for distributed memory systems as each grid point can be analyzed independently. A masking function provides the geometry definition for the Brinkman Penalization Method (BPM), where solid obstacles are modelled as porous media.

Brinkman penalization has several drawbacks, including limited control over boundary conditions. Dirichlet conditions are easily implemented, but the definition of Neumann conditions is severely limited. Furthermore, steep gradients at the solid interface can become problematic. To overcome these issues, a characteristic-based volume penalization method is proposed, allowing for general Dirichlet and Neumann boundary conditions to be defined at the interface.

Dedication

To my grandfather, Howard Brown.

Acknowledgements

First and foremost, I would like to thank my advisor, Prof. Oleg V. Vasilyev, for his guidance and support, and enough faith to keep me onboard beyond this Thesis.

I would like to thank the members of my research group, Nurlybek Kasimov, Alireza Nejadmalayeri, Scott Reckinger, Shannon Reckinger and Mike Pryor for the discussions and help.

Thanks to my friends and family for their support. I would also like to thank Romana Popara for her endless patience and encouragement.

Contents

Chapter

1	Introduction	1
1.1	Motivation and Objective	1
1.2	Methodology	2
1.3	Organization	4
2	Background	5
2.1	Aeroacoustics	5
2.1.1	Classical Acoustics	5
2.1.2	Aeroacoustic Analogy	8
2.2	Governing Equations	10
2.2.1	Conservation Laws	10
2.2.2	Ffowcs Williams and Hawkings Method	11
2.3	Computational Methodologies	13
2.3.1	Adaptive Wavelet Collocation	13
2.3.2	Brinkman Penalization	16
2.3.3	Generation and Incorporation of Complex Geometry	18
2.3.4	Non-reflective Boundary Conditions	20
2.3.5	Ffowcs-Williams Hawkings Analysis	23

3	Parallelization of Ray-Tracing Algorithm and Aeroacoustic Analogy	25
3.1	Extension of CAD Model Analysis Algorithm to Parallel Computers	25
3.1.1	Optimization of Ray-Tracing for Structured, Multi-Resolution Grid	25
3.1.2	Ray-Tracing for Parallel Computing	26
3.1.3	Results and Discussion	27
3.2	Parallel Implementation of Ffowcs-Williams Hawkings Integration Surface	28
3.2.1	Review of Serial Interface	28
3.2.2	FWH parallel Interface	28
3.2.3	Results and Discussion	29
4	Characteristic-Based Volume Penalization Method	32
4.1	Characteristic-Based Volume Penalization	32
4.1.1	Penalized Navier-Stokes Equations	34
4.2	Stability and Artificial Viscosity	36
4.3	Error Estimation From Acoustic Theory	37
4.4	Asymptotic Analysis	37
4.4.1	Asymptotic Analysis of the Fluid Region	38
4.4.2	Asymptotic Analysis of the Penalized Region	39
4.4.3	Asymptotic Analysis of Error Convergence	40
4.5	Results and Discussion	41
4.5.1	Benchmark Problem I: One Dimensional Heat Conduction	41
4.5.2	Benchmark Problem II: One Dimensional Normal Wave	43
4.5.3	Benchmark Problem III: Acoustic Scattering of a Single Source	46
4.5.4	Benchmark Problem IV: Incompressible Flow Past a Circular Cylinder	50
4.5.5	Benchmark Problem V: Vortex Shedding from a Circular Cylinder	51
5	Conclusions and Future Research	53
5.1	Conclusions	53

5.2 Future Research	53
-------------------------------	----

Bibliography	55
---------------------	----

Tables

Table

4.1	Numerical results for incompressible flow past a 2D cylinder at $Re = 40$	51
-----	---	----

Figures

Figure

3.1	Grid adapted to solid obstacle comprised of elliptical and circular entities.	30
3.2	CPU time of CAD analysis and number of grid points at every timestep.	30
3.3	Strong scaling of CAD algorithm.	31
3.4	Strong scaling for writing of FWH integration surface to file.	31
4.1	Time-averaged L_2 norm error for converging η_c and η_b	42
4.2	Fully reflected pressure waves for a high resolution penalized case, a case with artificial viscosity added near the solid interface, and the analytical solution.	44
4.3	Time-averaged L_2 norm error for converging η_c and η_b with Euler terms removed. . .	45
4.4	Time-averaged L_2 norm error for converging η_c and η_b	46
4.5	Error convergence for 1D acoustic reflection with artificial viscosity introduced at the solid interface.	47
4.6	Layout of 2D acoustic scattering problem. A solid obstacle is located at the origin, and pressure waves propagate from a source centered at $(4, 0)$	48
4.7	Time histories of pressure perturbations at several locations.	49
4.8	Force coefficients at $Re = 150$	52

Chapter 1

Introduction

1.1 Motivation and Objective

The problem of flow-generated noise is of increasing engineering significance in the modern world. It was engine noise by jet aircraft that motivated Sir James Lighthill to derive the first aeroacoustic analogy in the middle of the 20th century [15]. Any situation with unsteady flow produces an acoustic field, and in some cases, this can be quite significant. In aviation, automotive, and transportation industries, noise pollution adversely affects passenger comfort and is of concern to the surrounding communities. There are even aeroacoustic considerations for the energy industry. With wind turbines' increased popularity, noise generation impacts site selection.

In some cases, the impact of flow noise goes beyond discomfort, and can affect technological performance. In the marine environment where acoustic sensing is paramount, such as sonar mapping or undersea warfare, anticipating and eliminating self-generated sound interference becomes a mission critical concern. Noise generated by a sensing platform at frequencies of interest is detrimental to performance. Furthermore, flow noise from propellers and hull/airframe protrusions adversely affects platform stealth for both aviation and marine platforms. Characterization and prediction of aeroacoustic spectra can aid in the mitigation process from the earliest design stages.

Many aeroacoustic problems of practical significance arise from flow past complex bodies. Therefore, there is a need to develop effective computational tools to accurately simulate flow around arbitrary shapes. Difficulties manifest in generating realistic geometries and integrating them into a solver environment. Computational meshing of applied geometry tends to contribute

heavily to the computational cost of a numerical solution. Additionally, particular care must be given to the quality of the flow model itself. Minimizing the size of a computational domain, and therefore constructing is paramount in developing efficient models. Introduction of artificial computational boundaries can become a source of nonphysical structures within the flow. Because of a solution’s aeroacoustic sensitivity to spurious fluctuations in pressure, implementing nonreflecting boundary conditions is particularly important.

The objective of this thesis is to develop an efficient simulation methodology for flow around complex geometries, with an emphasis on acoustic solutions. One of the primary difficulties associated with external flow is the introduction of solid obstacles. While body-conformal meshes are straightforward in their treatment of boundary conditions, effective meshing can be quite costly. Immersed boundary methods eliminate the need for body fitting, and are even suitable for rectangular grids. The Brinkman Penalization Method (BPM) has been shown to be quite effective for a wide range of fluid problems [25, 3], including computational aeroacoustics [2, 22]. Originally applied to incompressible flows, Brinkman penalization has been effectively extended to fully compressible, viscous regimes [21].

However, there are several drawbacks to BPM, including the lack of generality in defining Neumann boundary conditions. Furthermore, steep gradients can cause computational difficulties requiring changes in the differencing stencil [2] or diffuse interfaces [25]. To overcome these difficulties, a new volume penalization method is proposed for the introduction of solid obstacles within the flow. This method provides general treatment for Neumann conditions, making the method suitable for a wide variety of fluid and non-fluid simulation.

1.2 Methodology

Computational aeroacoustics is fundamentally rooted in determining the time-accurate solution of a flow regime. Here, external compressible flow is considered around an obstacle of arbitrary shape. External flow is applicable to a wide variety of systems of engineering interest. One practical difficulty of such a problem lies in the scarcity of time and computational resources. External flows

often contain multiple temporal and spatial scales to be resolved. Efficient computation requires a grid that adapts automatically to resolve local scales and is able to follow the transient structures. Often, this can involve re-meshing steps that can be quite expensive.

The adaptive nature of wavelet modelling lends itself well to an efficient multi-resolution grid. Use of wavelet based adaptation has shown to be effective in a wide variety of fluid models [25, 26, 36], including compressible external flows [17]. The Adaptive Wavelet Collocation Method (AWCM) is used here to resolve multiple scales present in the solution.

Since AWCM utilizes a rectilinear grid, it precludes body-conformal grids for modelling solid obstacles. The use of conformal meshing is also undesirable in that the computational costs for effective grid generation are often quite high. Alternatively, immersed boundary methods are used here. A new characteristic-based volume penalization (CBVP) method is proposed here to model solid obstacles and overcome difficulties associated with Brinkman penalization. The error of CBVP can be rigorously controlled, making it appropriate for the high accuracies needed for aeroacoustic simulation.

For the prediction of flow generated noise, there are two principle methods of computational aeroacoustic modelling [37]. Direct methods calculate the sound concurrently with the flow field solution, accurately resolving acoustic scales on the computational mesh. This method has high computational costs associated with the acoustic scales, as well as requiring a domain that physically encompasses the radiation field of interest. Often, the sound-generating structures in the flow are limited to a region that is compact in comparison to the radiation distances of interest. Hybrid methods, using aeroacoustic analogy, separate the calculation of aeroacoustic source structures with that of the far-field sound. An accurate solution to the flow field only needs to encompass sound-generating structures. Acoustic analogy determines the propagation of acoustic waves from the flow solution. Hybrid methods assume a one-way decoupling of the acoustic and flow solutions, where the flow generates acoustic waves but these waves do not affect the flow. A popular aeroacoustic analogy for an external flow regime containing solid obstacles is the Ffowcs-Williams and Hawkings analogy. To circumvent errors associated with finite time intervals, a method has been developed

by Lockard to solve the Ffowcs-Williams and Hawkings equation in the frequency domain [23].

Acoustics solutions themselves are of a higher order than aerodynamic solutions. As such, aeroacoustic methods are particularly sensitive to spurious waves in the computational domain. The treatment of boundary conditions, especially in external flow, can be a major cause of non-physical reflections. Fluid modelling constantly pursues transparent boundaries that allow flow structures to exit the domain unimpeded. Freund has developed a zonal method for nonreflecting boundaries that introduces artificial damping and convective terms to the governing equations in the proximity of the domain edges [11]. The strength of the method lies in its computationally simple approach to maintaining the integrity of the solution in the physical portion of the computational domain, particularly for aeroacoustic applications.

1.3 Organization

The rest of this thesis is organized as follows. Chapter 2 outlines the necessary background for aeroacoustics and the methods used along with the dominant physics and constitutive equations. The computational methodologies used for nonreflective boundary conditions, solid obstacle modelling, and aeroacoustic analysis are described. Chapter 3 discusses the extension of automated CAD geometry analysis and aeroacoustic analogy for parallel computing. Finally, a new characteristic-based volume penalization method is introduced in Chapter 4. This method is inspired by the Brinkman penalization method, but allows for greater control over specific immersed boundary conditions. In this chapter, a series of single- and multi-dimensional benchmark problems are used to validate the new penalization method and the complete aeroacoustic solver environment. The final chapter outlines conclusions and comments upon future research on this topic.

Chapter 2

Background

2.1 Aeroacoustics

2.1.1 Classical Acoustics

In linear acoustic theory, acoustic waves are considered pressure solutions of the inhomogeneous wave equation,

$$\left(\frac{1}{c_0^2} \frac{\partial^2}{\partial t^2} - \nabla^2 \right) p = \mathcal{F}(\mathbf{x}, t), \quad (2.1)$$

where $\mathcal{F}(\mathbf{x}, t)$ is any generalized source, or collection of sources, in space and time. Solutions of the wave equation without the presence of solid boundaries are built upon the free space Green's function

$$G(\mathbf{x}, \mathbf{y}, t - \tau) = \frac{1}{4\pi|\mathbf{x} - \mathbf{y}|} \delta \left(t - \tau - \frac{|\mathbf{x} - \mathbf{y}|}{c_0} \right). \quad (2.2)$$

In three dimensions, this is an expanding sphere centered at \mathbf{y} , and zero for any time $t < \tau$. The Green's function is impulsive and nonzero only at the distance $r = |\mathbf{x} - \mathbf{y}|$ from the center \mathbf{y} . As the solution of the wave equation, it is the wave, propagating outward at velocity c_0 , instigated by an impulsive point source $\delta(\mathbf{x} - \mathbf{y}) \delta(t - \tau)$ located at $\mathbf{x} = \mathbf{y}$, and triggered at time $t = \tau$. As a solution to (2.1), the differential form of Green's function is

$$\left(\frac{1}{c_0^2} \frac{\partial^2}{\partial t^2} - \nabla^2 \right) G = \delta(\mathbf{x} - \mathbf{y}) \delta(t - \tau). \quad (2.3)$$

If we consider that any general source term $\mathcal{F}(\mathbf{x}, t)$ of (2.1) can be taken as the sum of a collection of impulsive point sources,

$$\mathcal{F}(\mathbf{x}, t) = \int \int_{-\infty}^{\infty} \mathcal{F}(\mathbf{y}, \tau) \delta(\mathbf{x} - \mathbf{y}) \delta(t - \tau) d^3\mathbf{y} d\tau, \quad (2.4)$$

then the Green's function can be used to construct the solution. In this way, the acoustic radiation is the linear superposition of impulsive point disturbances in pressure, given as

$$\begin{aligned} p(\mathbf{x}, t) &= \int \int_{-\infty}^{\infty} \mathcal{F}(\mathbf{y}, \tau) G(\mathbf{x}, \mathbf{y}, t - \tau) d^3\mathbf{y} d\tau \\ &= \frac{1}{4\pi} \int \int_{-\infty}^{\infty} \frac{\mathcal{F}(\mathbf{y}, \tau)}{|\mathbf{x} - \mathbf{y}|} \delta\left(t - \tau - \frac{|\mathbf{x} - \mathbf{y}|}{c_0}\right) d^3\mathbf{y} d\tau \\ &= \frac{1}{4\pi} \int_{-\infty}^{\infty} \frac{\mathcal{F}\left(\mathbf{y}, t - \frac{|\mathbf{x} - \mathbf{y}|}{c_0}\right)}{|\mathbf{x} - \mathbf{y}|} d^3\mathbf{y}. \end{aligned} \quad (2.5)$$

Acoustic waves are generally thought of as perturbations from the mean flow variables. For this reason, and given the impulsive nature of the Green's function, it is useful to introduce a more intuitive form of acoustic variables, where

$$\begin{aligned} \rho' &= \rho - \rho_0 \\ p' &= p - p_0. \end{aligned}$$

Since the undisturbed state (p_0, ρ_0) is typically constant, solutions to the wave equation are the nonzero perturbations propagating through the medium.

In classical acoustics, the generation of waves in fluids is attributed to a few distinct phenomena, or sources. These phenomena are, individually and collectively, sources $\mathcal{F}(\mathbf{x}, t)$ to the linear wave equation (2.1) [19]. The first of these is the simple, or monopole, source consisting of a time varying fluctuation of mass at a point, $q(t)\delta(\mathbf{x})$. For a monopole source at the origin, the forcing of the wave equation is the unsteady mass flux

$$\mathcal{F} = -q(t)\delta(\mathbf{x}). \quad (2.6)$$

The radiated pressure waves take on the form

$$p(\mathbf{x}, t) = -\frac{q\left(t - \frac{|\mathbf{x}|}{c_0}\right)}{4\pi|\mathbf{x}|}, \quad (2.7)$$

and

$$p'(\mathbf{x}, t) = \frac{1}{4\pi} \int_{-\infty}^{\infty} \frac{q\left(\mathbf{y}, t - \frac{|\mathbf{x}-\mathbf{y}|}{c_0}\right)}{|\mathbf{x} - \mathbf{y}|} d^3\mathbf{y}, \quad (2.8)$$

for a point and distributed source, respectively. The radiation of acoustic waves from a simple source is nondirectional in nature.

The second source can be thought of as the summation of two monopole sources an infinitesimal distance apart. If the strengths of these sources are equal and opposite, the net mass flux is zero and the total monopole strength is zero. However, the wave equation is still satisfied, with the source term taking on the form of an unsteady force acting upon the fluid. A dipole source consisting of a volume force acting in the j th direction at the origin,

$$\mathcal{F} = \nabla \cdot (\mathbf{F}(t)\delta(\mathbf{x})) = \frac{\partial F_j(t)\delta(\mathbf{x})}{\partial x_j}, \quad (2.9)$$

will create acoustic pressure perturbations

$$p'(\mathbf{x}, t) = \frac{\partial}{\partial x_j} \left(\frac{F_j\left(t - \frac{|\mathbf{x}|}{c_0}\right)}{4\pi|\mathbf{x}|} \right). \quad (2.10)$$

The solution for a distribution of dipoles is

$$p'(\mathbf{x}, t) = \frac{1}{4\pi} \frac{\partial}{\partial x_j} \int_{-\infty}^{\infty} \frac{F_j\left(\mathbf{y}, t - \frac{|\mathbf{x}-\mathbf{y}|}{c_0}\right)}{|\mathbf{x} - \mathbf{y}|} d^3\mathbf{y}. \quad (2.11)$$

The radiation field of the dipole source is a bi-directional figure eight pattern in the direction of the acting force. Considering the dipole as the sum of two infinitesimally close opposing monopoles, it is rightly expected that the strength of a dipole is significantly less than the sum of the two individual monopoles. The dipole is a less efficient radiator of energy. Dipoles exist whenever fluctuating forces exist in the fluid, and are often marked by the presence of solid objects. Vibration of machinery or structures creates dipole acoustic radiation.

The third fundamental source can be thought of as the result of two opposing dipoles superimposed an infinitesimal distance apart. The net force at any given instance is zero. However, the effect of the nonzero stresses from the dipole summation will still provide forcing for a solution to

the wave equation. The quadrupole source is the volumetric stress

$$\mathcal{F}(\mathbf{x}, t) = \frac{\partial^2 T_{ij}(\mathbf{x}, t)}{\partial x_i \partial x_j}. \quad (2.12)$$

The pressure fluctuations for a point and distributed quadrupole are

$$p'(\mathbf{x}, t) = \frac{\partial^2}{\partial x_i \partial x_j} \frac{T_{ij} \left(t - \frac{|\mathbf{x}|}{c_0} \right)}{4\pi |\mathbf{x}|} \quad (2.13)$$

and

$$p'(\mathbf{x}, t) = \frac{1}{4\pi} \frac{\partial^2}{\partial x_i \partial x_j} \int_{-\infty}^{\infty} \frac{T_{ij} \left(\mathbf{y}, t - \frac{|\mathbf{x}-\mathbf{y}|}{c_0} \right)}{|\mathbf{x}-\mathbf{y}|} d^3 \mathbf{y}. \quad (2.14)$$

Quadrupoles radiate in a cloverleaf pattern, and their strength is less than the combined strength of the constitutive dipoles, for the same reasons as before. The efficiency of a dipole as an acoustic source is less than that of the monopole or dipole.

Since higher order sources are still less efficient, discussion typically stops at the quadrupole. Many aeroacoustic analogies, including the Ffowcs Williams and Hawkings equation, only consider the effects of monopole, dipole, and quadrupole sources.

2.1.2 Aeroacoustic Analogy

Aeroacoustic analogies are based upon reformulation of the constitutive flow equations, $\mathcal{N}(\mathbf{q}) = 0$, into a form analogous of a wave equation. The general form of aeroacoustic analogies follows

$$\mathcal{L}(\mathbf{q}) = \mathcal{S}(\mathbf{q}),$$

where \mathbf{q} is the set of variables that comprise the solution of the flow equations, \mathcal{L} is a wave operator, and \mathcal{S} is analogous to the corresponding source terms [37]. The various aeroacoustic analogies differ in the form of the wave operator \mathcal{L} . The obvious shortcoming, as pointed out by multiple authors [15, 37] is that the wave operator \mathcal{L} and the sources \mathcal{S} are both functions of the flow variables \mathbf{q} . The propagation is part of the same flow regime from which it is sourced. In this respect, it is not precisely a wave equation, but rather analogous. A principle assumption with aeroacoustic analogy

is that there is a one-way decoupling of the acoustics from the flow. The flow field generates the acoustic perturbations, but the perturbations themselves do not affect the flow [15].

The most famous, and historically earliest, of the aeroacoustic analogies was derived by Lighthill in 1952, specifically motivated by the problem of jet noise and was built around a steady free jet in a quiescent fluid [18]. In Lighthill's analogy, continuity and momentum equations are rearranged into the form of the linear wave equation (2.1):

$$\left(\frac{\partial^2}{\partial t^2} - c_0^2 \nabla^2 \right) \rho = \frac{\partial^2 T_{ij}}{\partial x_i \partial x_j}, \quad (2.15)$$

where

$$T_{ij} = \rho u_i u_j + (p - c_0^2 \rho) \delta_{ij} - \sigma_{ij}. \quad (2.16)$$

Noting that $c_0^2 = \partial p / \partial \rho$ and $p' = p - p_0$, the more familiar form of the acoustic wave equation emerges:

$$\left(\frac{1}{c_0^2} \frac{\partial^2}{\partial t^2} - \nabla^2 \right) p' = \frac{\partial^2 T_{ij}}{\partial x_i \partial x_j}. \quad (2.17)$$

In this form, Lighthill has assumed that there are no solid obstacles in the flow and that there is no net fluctuation in mass. The result is that his aeroacoustic analogy describes unbounded flow in a quiescent state, where the stress tensor T_{ij} describes a quadrupole source. The form of the solution is straightforward, as shown in equation (2.14), however complete knowledge of the flow is needed to define the source, T_{ij} .

Williams and Hawkings extended this analogy to include the presence of surfaces in the flow. With an arbitrary surface, monopole and dipole sources emerge, accounting for the possible presence of solid obstacles.

Solving aeroacoustic analogies requires time-accurate knowledge of the flow regime. Because of the difficulty in obtaining analytical solutions to problems of engineering interest, accurate computational solutions of the flow field are often well suited for prediction of aeroacoustic noise.

2.2 Governing Equations

The problem considered is external flow of a compressible, viscous fluid surrounding obstacles O_i on \mathbb{R}^2 or \mathbb{R}^3 in two or three dimensions. The solution is found in Cartesian coordinates on a domain, $\Omega = [L_1, L_2] \times [M_1, M_2]$, containing all obstacles O_i . A hybrid approach to predicting the flow-generated sound is used, where the aeroacoustic solution is calculated after the transient flow has been determined. Direct numeric simulation (DNS) of the constitutive equations is used for the low Reynolds number flows simulated here.

2.2.1 Conservation Laws

The fluid flow is governed by the compressible Navier-stokes equations. For a domain with position vector \mathbf{x} and fluid velocity \mathbf{u} , the continuity, momentum and energy equations in conservative form are

$$\frac{\partial \rho}{\partial t} = -\frac{\partial \rho u_j}{\partial x_j}, \quad (2.18)$$

$$\frac{\partial \rho u_i}{\partial t} = -\frac{\partial (\rho u_i u_j)}{\partial x_j} - \frac{\partial p}{\partial x_i} + \frac{\partial \tau_{ij}}{\partial x_j}, \quad (2.19)$$

$$\frac{\partial \rho e}{\partial t} = -\frac{\partial}{\partial x_j} [(\rho e + p) u_j] + \frac{\partial (u_i \tau_{ij})}{\partial x_j} + \frac{\partial}{\partial x_j} \left(k \frac{\partial T}{\partial x_j} \right), \quad (2.20)$$

where ρ is the density of the fluid, ρu_i is the mass flux, p is the pressure, and k is the thermal conductivity. The shear stress tensor is

$$\tau_{ij} = \mu \left(\frac{\partial u_i}{\partial x_j} + \frac{\partial u_j}{\partial x_i} - \frac{2}{3} \frac{\partial u_k}{\partial x_k} \delta_{ij} \right),$$

and the total specific energy is

$$e = \frac{1}{2} u_i u_i + c_p T - \frac{p}{\rho},$$

where $p = \rho R T$, the gas constant is $R = c_p(\gamma - 1)/\gamma$, the specific heat ratio is $\gamma = \frac{c_p}{c_v}$, and μ is the dynamic viscosity.

For the computational model, the nondimensionalized Navier-Stokes equations corresponding

to (2.18), (2.19) and (2.20) are

$$\frac{\partial \rho^*}{\partial t^*} = -\frac{\partial \rho^* u_j^*}{\partial x_j^*}, \quad (2.21)$$

$$\frac{\partial \rho^* u_i^*}{\partial t^*} = -\frac{\partial(\rho^* u_i^* u_j^*)}{\partial x_j^*} - \frac{\partial p^*}{\partial x_i^*} + \frac{1}{Re_a} \frac{\partial \tau_{ij}^*}{\partial x_j^*}, \quad (2.22)$$

$$\frac{\partial \rho^* e^*}{\partial t^*} = -\frac{\partial}{\partial x_j^*} [(\rho^* e^* + p^*) u_j^*] + \frac{1}{Re_a} \frac{\partial(u_i^* \tau_{ij}^*)}{\partial x_j^*} + \frac{1}{(\gamma - 1)} \frac{1}{Re_a Pr} \frac{\partial}{\partial x_j^*} \left(\mu \frac{\partial T^*}{\partial x_j^*} \right), \quad (2.23)$$

where

$$\begin{aligned} p^* &= \frac{\rho^* T^*}{\gamma}, \\ \tau_{ij}^* &= \mu^* \left(\frac{\partial u_i^*}{\partial x_j^*} + \frac{\partial u_j^*}{\partial x_i^*} - \frac{2}{3} \frac{\partial u_k^*}{\partial x_k^*} \delta_{ij} \right), \\ e^* &= \frac{1}{2} u_i^* u_i^* + c_p T^* - \frac{p^*}{\rho^*}, \end{aligned}$$

Re_a is the acoustic Reynolds number and Pr is the Prandtl number. Length scales are based on the characteristic length of the obstacle, L . The velocity \mathbf{u} is nondimensionalized based on the reference speed of sound c_0 , time based on L/c_0 , specific energy on c_0^2 , density on ρ_0 , pressure on $\rho_0 c_0^2$, viscosity on μ_0 , thermal conductivity on $\mu_0 c_{p0}$, and temperature on T_0 . Note that nondimensional pressure p^* is not based on a reference pressure p_0 .

2.2.2 Ffowcs Williams and Hawkings Method

In this nondirect approach, the acoustic scales and radiation are not resolved for concurrently with the flow solution. Instead, the sound radiation is treated via acoustic analogy. The Ffowcs Williams and Hawkings equation is solved across the computational domain using the time accurate solution as the source.

The Ffowcs Williams and Hawkings (FWH) aeroacoustic analogy is applied to a flow regime in \mathbb{R}^3 containing a rigid closed surface S . A volume function f is prescribed by the surface, where

$$f(t) = \begin{cases} f > 0 & \text{outside } S \\ f < 0 & \text{inside } S \end{cases}$$

Likewise, the Heaviside function is described by $H(f) = 1$ for $f > 0$ and $H(f) = 0$ for $f < 0$. The spatial derivative, $\partial f / \partial x_i$ is nonzero only upon the surface, S [15].

Under these conditions, and considering fluxes in flow variables across S , the continuity and momentum equations can exactly be rearranged into the differential forms

$$\left(\frac{\partial^2}{\partial t^2} - c_0^2 \nabla^2 \right) (H(f)\rho) = \frac{\partial^2 (T_{ij}H(f))}{\partial x_i \partial x_j} - \frac{\partial (F_i \delta(f))}{\partial x_i} + \frac{\partial (Q \delta(f))}{\partial t}, \quad (2.24)$$

where T_{ij} again is the Lighthill stress tensor (2.16). In comparing the source terms of equation (2.24) with the fundamental acoustic sources, (2.6) (2.9), we find that the dipole term is

$$F_i = (P_{ij} + \rho u_i (u_j - v_j)) \frac{\partial f}{\partial x_i}$$

and a monopole is given by

$$Q_i = (p_0 v_i + \rho (u_i - v_i)) \frac{\partial f}{\partial x_i},$$

where \mathbf{v} is the velocity of the surface S and P_{ij} is the compressive stress tensor. As in Lighthill's analogy (2.17), we see that $T_{ij}H(f)$ describes a quadrupole outside of the surface S . Additionally, F_i describes a dipole on S and Q_i a monopole on S . Using the Green's function, the retarded potential solution of the Ffowcs Williams and Hawkings equation, given in acoustic perturbation quantities, is

$$\begin{aligned} p'(\mathbf{x}, t) = & \frac{1}{4\pi} \frac{\partial^2}{\partial x_i \partial x_j} \int_V \frac{T_{ij}(\frac{|\mathbf{x}-\mathbf{y}|}{c_0})}{|\mathbf{x}-\mathbf{y}|} d^3 \mathbf{y} \\ & - \frac{1}{4\pi} \frac{\partial}{\partial x_i} \int_S \frac{F_i(\frac{|\mathbf{x}-\mathbf{y}|}{c_0})}{|\mathbf{x}-\mathbf{y}|} d^2 \mathbf{y} \\ & + \frac{1}{4\pi} \frac{\partial}{\partial t} \int_S \frac{Q_i(\frac{|\mathbf{x}-\mathbf{y}|}{c_0})}{|\mathbf{x}-\mathbf{y}|} d^2 \mathbf{y}. \end{aligned} \quad (2.25)$$

In two dimensions, the solution (2.25) simply reflects the use of the appropriate two dimensional Green's function [23]. The monopole and dipole sources on the surface S are the result of the changing volume enveloped by S and the unsteady forces present along the boundary. The integral across the stress tensor T_{ij} considers the perturbations caused by shear stresses in the volume outside of the surface. It is important to note that shear stresses within S manifest as lower order sources on S [23].

In many practical cases, the FWH equation can be simplified by assuming that the surface is stationary and constant volume in \mathbf{x} . In such a case, the monopole source in (2.25) vanishes, and the dipole source F_i is simplified. Under these assumptions, the FWH analogy is known as Curle's equation [15].

Typically, we are concerned with noise that propagates large distances from the sources. In this case, the observer is located a distance that is many wavelengths away from the source region. Further assuming that the source region is compact, where the distance from the observer $|\mathbf{x} - \mathbf{y}|$ is large compared to the length scale of the source region, Curle's equation for the acoustic far-field becomes

$$p'(\mathbf{x}, t) \approx \frac{1}{4\pi} \frac{\partial^2}{\partial x_i \partial x_j} \int_V \frac{T_{ij}(\frac{|\mathbf{x}-\mathbf{y}|}{c_0})}{|\mathbf{x}|} d^3\mathbf{y} - \frac{1}{4\pi} \frac{\partial}{\partial x_i} \int_S \frac{F_i(\frac{|\mathbf{x}|}{c_0})}{|\mathbf{x}-\mathbf{y}|} d^2\mathbf{y}. \quad (2.26)$$

2.3 Computational Methodologies

2.3.1 Adaptive Wavelet Collocation

Aeroacoustic problems, and many general fluid problems, contain many disparate temporal and spatial scales. For such problems, solving on a constant resolution mesh is inefficient. High resolutions are only needed at locations where sharp transitions occur. In regions with gradual spatial variation, only a coarse mesh is needed to adequately resolve the solution. Furthermore, disparate structures are often transient, moving throughout the domain and requiring an adaptive grid to continuously resolve dissimilar scales.

The adaptive wavelet collocation method (AWCM) is a technique for dynamically adapting the grid to local scales by means of [32, 33, 34, 35]. A solution, $u(\mathbf{x})$, on a discrete grid is approximated using a set of wavelets, where there is a one-to-one correspondence between grid points and wavelets. Filtering out insignificant wavelets from the computational domain can greatly compress the number of grid points, while still rigorously maintaining desired accuracy.

Second generation wavelets are used in AWCM, where translational/dilational relationships

between wavelets and a mother wavelet have been abandoned [34]. First, consider a set of points \mathbf{x} on a closed interval Ω that form a set of \mathcal{J} nested grids,

$$\mathcal{G}^j = \{x_k^j \in \Omega : k \in \mathcal{K}^j\}, j \in \mathcal{J}. \quad (2.27)$$

By enforcing $x_k^j = x_{2k}^{j+1}$, the nestedness of the grids, $\mathcal{G}^j \subset \mathcal{G}^{j+1}$, is ensured. By desired scaling functions $\phi_k^j(\mathbf{x})$ and wavelets $\psi_l^j(\mathbf{x})$, a function $u(\mathbf{x})$ can be decomposed [34] by

$$u(\mathbf{x}) = \sum_{k \in \mathcal{K}^0} c_k^0 \phi_k^0(\mathbf{x}) + \sum_{j=0} \sum_l d_l^j \psi_l^j(\mathbf{x}). \quad (2.28)$$

By truncating the summation over the j_{th} index at some upper resolution level \mathcal{J} , the function $u(\mathbf{x})$ is approximated by $u^{\mathcal{J}}(\mathbf{x})$. The wavelet coefficients, d_l^j , are representative of that wavelet's contribution to the solution. Eliminating wavelets whose coefficients fall below some *a priori* threshold ϵ allows for a large number of points to be disregarded, while only incurring an error of $O(\epsilon)$. The remaining set comprises the significant wavelets, defined as those having a coefficient above the threshold value, that is $|d_l^j| \geq \epsilon$.

To examine the error incurred in the wavelet approximation, we group the wavelets in equation (2.28) into those above and below the threshold ϵ ,

$$u(\mathbf{x}) = u_{\geq}(\mathbf{x}) + u_{<}(\mathbf{x}). \quad (2.29)$$

From the wavelet transform, (2.28), the wavelet groups are

$$u_{\geq}(\mathbf{x}) = \sum_{k \in \mathcal{K}^0} c_k^0 \phi_k^0(\mathbf{x}) + \sum_{j=0} \sum_{\substack{l \\ |d_l^j| \geq \epsilon}} d_l^j \psi_l^j(\mathbf{x}), \quad (2.30)$$

$$u_{<}(\mathbf{x}) = \sum_{j=0} \sum_{\substack{l \\ |d_l^j| < \epsilon}} d_l^j \psi_l^j(\mathbf{x}). \quad (2.31)$$

From these relationships, it can be shown [9, 33, 34] that

$$|u(\mathbf{x}) - u_{\geq}(\mathbf{x})| \leq C_1 \epsilon \leq C_2 N^{-p/n}, \quad (2.32)$$

where N is the number of significant wavelets, p is the order of the wavelets, and n is the dimensionality of the problem. The coefficients C_1 and C_2 are dependent upon the function $u^{\mathcal{J}}(\mathbf{x})$, but are $O(1)$.

To realize domain compression and adaptation, we acknowledge that each grid point \mathbf{x} uniquely corresponds to a collocation point for a wavelet. Since $u(\mathbf{x})$ can be approximated by $u_{\geq}(\mathbf{x})$ on an N number of wavelets, all non-significant wavelets and their corresponding grid points can be discarded. The result is a nested set of computational grids $\mathcal{G}_{\geq}^{\mathcal{J}} \subset \mathcal{G}^{\mathcal{J}}$ where $\mathcal{G}^{j+1} \subset \mathcal{G}^j$ with areas of high resolution clustered about regions of sharp transition in $u(\mathbf{x})$. The nature of the adaptive grid $\mathcal{G}_{\geq}^{\mathcal{J}}$ is highly dependent upon $u(\mathbf{x})$.

For transient problems, the grid $\mathcal{G}_{\geq}^{\mathcal{J}}(t)$ is time dependent. As the solution evolves, regions of sharp local structures may change position in Ω , and in order to maintain accuracy, changes in $u(\mathbf{x})$ are anticipated by adding the nearest neighbouring points of significant wavelets to the grid $\mathcal{G}_{\geq}^{\mathcal{J}}$ [32].

Based upon the compression and interpolation properties of wavelets, the numerical algorithm for adapting the grid to a transient solution proceeds in a straightforward fashion[34]:

- (1) The solution $u^{\mathcal{J}}(t)$ is known from a previous timestep or the initial conditions, and exists on $\mathcal{G}_{\geq}^{\mathcal{J},t}$ for time t . Based on the magnitude of the wavelet coefficients in (2.28) and a given ϵ , the grid $\mathcal{G}_{\geq}^{\mathcal{J},t+\Delta t}$ is created to include nearest neighbours of \mathbf{x}_i^j for all $j > j^{\min}$.
- (2) If $\mathcal{G}_{\geq}^{\mathcal{J},t}$ and $\mathcal{G}_{\geq}^{\mathcal{J},t+\Delta t}$ are the same, proceed directly to step 3. Otherwise, the solution is interpolated for the new points in $\mathcal{G}_{\geq}^{\mathcal{J},t+\Delta t}$.
- (3) Integrate the differential system to obtain the new solution $u_{\geq}^{\mathcal{J}}(t + \Delta t)$ on $\mathcal{G}_{\geq}^{\mathcal{J},t+\Delta t}$, and go back to step 1.

Since a dyadic, nested grid is used, adaptation from j to $j + 1$ will resolve features at half the scale. With this adaptation scheme, AWCM not only achieves high compression of the computational grid, but the L^{∞} -norm error is strictly controlled. By prescribing a lower threshold, ϵ , and a sufficiently high \mathcal{J} to capture all significant wavelets, the error can be systematically reduced by including a higher number of wavelets. The adaptation algorithm itself, however, is computationally cheap and can be effectively implemented at every timestep.

2.3.2 Brinkman Penalization

Introduction of solid objects within the domain requires treatment of the domain and constitutive equations in the edges and body of the obstacle. Specified boundary conditions must be rigorously enforced along surfaces. Where body-fitting meshes are used, prescription of conditions proceeds in a natural fashion. However, meshing of arbitrarily complex geometry can be expensive, especially in an adaptive environment. Re-meshing and identifying surface nodes can comprise a large portion of the solution computational costs.

Immersed boundary methods have been developed to simulate the flow around arbitrary complex geometry on a non-body conformal grid. The Brinkman penalization method achieves this by penalizing the flow equations within the obstacle and modelling it as porous media. Porous media consists of a solid matrix with interconnected pores allowing fluid penetration. The volume fraction of pores in the media is the porosity ϕ . For a porosity $\phi \ll 1$, the media could be considered to resemble a solid obstacle.

The continuity equation for porous media follows naturally [21],

$$\frac{\partial \rho}{\partial t} = -\frac{1}{\phi} \frac{\partial \rho u_j}{\partial x_j}. \quad (2.33)$$

The momentum equation was first derived for incompressible flows, and later extended to the compressible regime. For porous media, Darcy's law for fluid momentum balances the fluid pressure p with viscous stresses [6],

$$\mathbf{v} = -\frac{K}{\mu} \nabla p, \quad (2.34)$$

where \mathbf{v} is the seepage velocity given by the Dupuit-Forchheimer relationship $\mathbf{v} = \phi \mathbf{u}$. Addition of a viscous term, Darcy's law is extended into the Brinkman equation [3],

$$\nabla p = -\frac{\mu}{K} \mathbf{v} + \mu \nabla^2 \mathbf{v}. \quad (2.35)$$

Combining the Brinkman and continuity equations into a form analogous of the incompressible Navier-Stokes equations [31] yields a conservative form of the momentum equation for fluid in a

porous media,

$$\frac{1}{\phi} \frac{\partial \rho v_i}{\partial t} = -\frac{1}{\phi} \frac{\partial}{\partial x_j} (\rho \phi^{-1} v_i v_j) - \frac{\partial p}{\partial x_i} + \mu \frac{\partial^2 v_i}{\partial x_j^2} - \frac{\mu}{K} v_i \quad (2.36)$$

where $\phi = \phi(\mathbf{x})$. Location dependent porosity is considered in order to model porous media flow in all of the domain, Ω , as obstacles within an open flow regime. For the region external to porous obstacles, ϕ is considered to be 1, and internal to the obstacles, $\phi \ll 1$. Liu notes several instances where the momentum equation (2.36) can be greatly simplified for use in numerical simulation [21].

Lastly, the energy equation for flow through porous media is simply the compressible energy equation (2.20) with a forcing term to maintain a specified temperature,

$$\frac{\partial \rho e}{\partial t} = -\frac{\partial}{\partial x_j} [(\rho e + p) v_j] + \frac{\partial}{\partial x_j} \left(k \frac{\partial T}{\partial x_j} \right) - \frac{h}{\phi} (T - T_0). \quad (2.37)$$

For simplicity, the heat transfer coefficient h is included in a normalized thermal permeability $\eta_T = \phi/h$.

In using these equations to adequately simulate obstacles in external flow, no-slip boundary conditions need to be strictly enforced for obstacles O_i ,

$$\mathbf{u} = \mathbf{U}_0 \text{ on } \partial O_i, \forall i, \quad (2.38)$$

where \mathbf{U}_0 is the obstacle velocity. Angot et al. [1] model this effect for incompressible flows by using Brinkman penalization with the L^2 -penalized equation

$$\frac{\partial u_i}{\partial t} = -\frac{\partial (u_i u_j)}{\partial x_j} - \frac{\partial p}{\partial x_i} + \nu \frac{\partial^2 u_i}{\partial x_j^2} - \frac{\chi}{\eta} (u_i - U_{0i}), \quad (2.39)$$

where permeability, $\eta = \alpha\phi$, is a constant normalized viscous permeability. A masking function, χ , is defined as

$$\chi = \begin{cases} 1 & \text{in } \mathbf{x} \in O_i, \\ 0 & \text{otherwise.} \end{cases}$$

Effectively, χ provides support for the permeability $\phi(\mathbf{x}) = \chi\phi$, imposing $\phi = 1$ outside of the obstacles.

Appropriate extension of Brinkman penalization to compressible regimes was achieved by Liu and Vasilyev [21]. In order to enforce no-slip conditions, the compressible Navier-Stokes equations

become

$$\frac{\partial \rho}{\partial t} = - \left[\mathbf{1} + \left(\frac{\mathbf{1}}{\phi} - \mathbf{1} \right) \chi \right] \frac{\partial \rho u_j}{\partial x_j}, \quad (2.40)$$

$$\frac{\partial \rho u_i}{\partial t} = - \frac{\partial (\rho u_i u_j)}{\partial x_j} - \frac{\partial p}{\partial x_i} + \frac{\partial \tau_{ij}}{\partial x_j} - \frac{\chi}{\eta} (\mathbf{u}_i - \mathbf{U}_{0i}), \quad (2.41)$$

$$\frac{\partial \rho e}{\partial t} = - \frac{\partial}{\partial x_j} [(\rho e + p) u_j] + \frac{\partial (u_i \tau_{ij})}{\partial x_j} + \frac{\partial}{\partial x_j} \left(k \frac{\partial T}{\partial x_j} \right) - \frac{\chi}{\eta \mathbf{T}} (\mathbf{T} - \mathbf{T}_0), \quad (2.42)$$

For a solid obstacle within a flow regime, equations (2.40), (2.41) and (2.42) are solved everywhere. More notably, the treatment of derivatives can be uniform across the entire domain. Efficient finite differencing schemes can be employed, providing a marked advantage over body-conformal meshes [1].

There are a few drawbacks associated with Brinkman penalization. The introduction of low porosity on the continuity equation can lead to steep gradients, requiring modifications of the differencing stencil within the fluid region [2] or the use of diffuse-edge masking functions [25]. Furthermore, the BPM is limited in the application of Dirichlet boundary conditions. The use of porosity ϕ mimics a no-flux boundary condition, but does not allow for application of general Neumann conditions. This makes Brinkman penalization in its current form unsuitable for simulations involving specified heat fluxes.

2.3.3 Generation and Incorporation of Complex Geometry

The use of penalization methods depends on a description of a mask function, χ , that accurately represents any arbitrary obstacle O_i . For simple geometry, this is readily accomplished through the use of analytical functions to describe surfaces. However, for problems of engineering interest, the complexity of the geometry can make it impractical or impossible to create a satisfactory masking function analytically, especially in three dimensions.

The use of CAD software to generate desired geometry is a practical recourse. Determining χ for a given discrete grid is the primary challenge to using CAD models. For a set of points \mathbf{P} in \mathbb{R} containing a closed surface S , it must be found whether the points are located inside ($\chi = 1$) or outside ($\chi = 0$) of S . Automated analysis of points constrained by an arbitrary surface is a problem

well known in computer graphics as well as in computational modelling. For in/out determination, consider a ray originating from point P_1 and extending to infinity. If the ray intersects S an even number of times, it is located outside, if it intersects S an odd number of times, it is inside. If there are zero intersections, the point is definitively outside. In theory, the direction of the ray can be arbitrary, and only one ray is needed. Ghosh argues that this principle, known as the odd-parity rule, has a basis in Gauss' Law and electromagnetic field theory [14].

For analyzing CAD geometry, a format that represents the surfaces of solid bodies is required. Consider then, a closed surface S represented by a piecewise continuous assembly of bounded analytical surfaces $s\{s_i\}$. Determination of point location is then based upon ray intersections with any $s_i \subset S$. Knowing the bounded points $\xi|_{s_i}$ that form the surface s_i , determination of intersections from an arbitrary ray follows naturally. In developing an algorithm, Schneider and Eberly suggest a parametric ray of the form

$$\mathbf{m} = \mathbf{P}(\mathbf{x}) + \tau \hat{\mathbf{m}},$$

where $\hat{\mathbf{m}}$ is the direction of ray [27]. If $\xi = f(\mathbf{x})$, and a τ can be found so that

$$\xi|_{s_i} = \mathbf{P}(\mathbf{x}) + \tau \hat{\mathbf{m}}, \quad (2.43)$$

for a specified $\hat{\mathbf{m}}$, then intersection is determined for \mathbf{m} with s_i . Particular care must be taken for rays that intersect nodes and edges of s_i , and experience shows that multiple rays are needed to ensure robust analysis.

Some standardized CAD formats include representation of geometric surfaces by using a mesh of complex polygons. For non-planar surfaces, fine resolution with a large number of polygons is used. Odd-parity algorithms are relatively simple for such a format, as $\xi|_{s_i}$ is planar and intersection easy to determine. As such, using poly-mesh representation is a popular method of computational analysis.

For universal representation of smooth contoured geometry, Initial Graphics Exchange Specification (IGES) files format is used. Aside from planar surfaces, IGES utilizes a wide variety of

circular, revolved, and B-spline curves to accurately represent curved surfaces. The principle advantage of this is that fewer surfaces are needed to represent complex geometry at a greater precision. This is advantageous in fluid modelling to guarantee sufficient resolution of the geometry. In using IGES format, the resolution of a surface is limited only by the resolution of the mesh, which can be defined or changed based on the needs of the simulation without requiring geometry regeneration.

A standard file format, IGES is not proprietary to modelling platforms. This format is ASCII based, or compressed version thereof, and contains descriptions of five classes of entities: curve and surface geometries, constructive solids, boundary represented solids, annotation entities, and structures [30]. The format is maintained as a specification by the US Product Data Association, and as such, is readily available and accessible for use in the computational environment.

2.3.4 Non-reflective Boundary Conditions

In addition to the immersed boundaries, the computational boundaries must also be well posed and representative of the physics of the external flow. Unlike internal flows, where physical boundaries readily define the domain, external flows are typically modeled as unbounded. Furthermore, to improve efficiency, the smallest practical domain is desired without introducing edge effects.

A practical computational domain is constructed by imposing artificial boundaries around flows of interest. To establish boundaries at a distance where flow structures have effectively dissipated to the undisturbed state would often be computationally impractical, if not impossible. In many cases, the desired flow characteristics lie in a much more compact region. In order to accurately simulate the physical system, the boundaries must therefore allow flow structures to propagate out without reflection of non-physical phenomena back into the domain.

In the case of aeroacoustic simulation, this is particularly important as sound computation is especially sensitive to spurious perturbations. The domain should only be large enough to capture structures that significantly contribute to aeroacoustic sourcing. Dynamically significant flow structures may arise that are not of aeroacoustic interest, and could be present near the domain

boundary. Such fluctuations could cause non-physical wave reflection if boundary conditions are not carefully established. Such spurious waves can easily interfere with the calculation of acoustic propagation [11].

2.3.4.1 Convection-Zone Boundary Conditions

In order to prescribe numerically transparent boundaries, the time-dependent solution must be fully defined along the domain edge. For external flows, this is not usually possible to do explicitly. For any transient hyperbolic system, such as the compressible Navier-Stokes equations, the behaviour along the boundary is described by outgoing waves as well as incoming waves from outside the domain. The outgoing waves are sufficiently defined by the interior solution, but the incoming waves have no such support. For a well posed problem, the precise behaviour of incoming waves must be determined, or at least sufficiently simulated [28].

Characteristic analysis of the one dimensional Euler equations [28] yields the eigenvalues

$$\lambda_1 = u - c, \lambda_2 = u, \lambda_3 = u + c,$$

which represent the propagation velocities of the characteristic waves, where u is the convective velocity and c is the speed of sound. Analogously applying these characteristics to the compressible Navier-Stokes equations, we examine them along an arbitrary boundary [24]. At an outflow boundary, we only want to pass internal structures out of the domain. For this boundary type, λ_2 and λ_3 are defined by the interior solution, and pose no direct complication to condition prescription. However, the incoming wave at velocity $u - c$ must be somehow treated. At an inflow boundary, it is desired to pass problem specific flow features into the domain while simultaneously allowing outgoing acoustic waves to propagate upstream. For a well posed inflow, we find that there are several boundary condition sets that are well posed [24]. The problem with explicit definition of flow variables is that they are rigid and will cause nonphysical reflections.

Poinsot and Lele dealt with boundary difficulties by proposing evolutionary conditions that approximate desired inflow and outflow behaviours based on approximations of characteristic wave

amplitude [24]. Another, mathematically simpler, method of approximating nonreflecting boundary treatments was proposed by Freund [11]. Freund's method is zonal-based, in that the computational domain is extended by a nonphysical buffer region. In this region, the flow is conditioned to provide nonreflecting support for the physical domain. The compressible Navier-Stokes equations are modified with the addition of two nonphysical terms within the boundary region [11],

$$\frac{\partial \rho}{\partial t} + \frac{\partial(\rho u_j)}{\partial x_j} + U(x_1) \frac{\partial \rho}{\partial x_1} = -\sigma(x_1)(\rho - \rho_0) \quad (2.44)$$

$$\frac{\partial(\rho u_i)}{\partial t} + \frac{\partial(\rho u_i u_j)}{\partial x_j} + U(x_1) \frac{\partial(\rho u_i)}{\partial x_1} = \frac{\partial \tau_{ij}}{\partial x_j} - \sigma(x_1)[\rho u_i - (\rho u_i)_0] \quad (2.45)$$

$$\frac{\partial(\rho e)}{\partial t} + \frac{\partial(\rho e u_j)}{\partial x_j} + U(x_1) \frac{\partial(\rho e)}{\partial x_1} = \frac{\partial(u_j \tau_{ij})}{\partial x_j} - \sigma(x_1)[\rho e - (\rho e)_0], \quad (2.46)$$

for boundaries in the normal x_1 direction.

In general, the artificial convection $U(x_1)$ is chosen so that $|U(x_1)| \geq c$. The artificial damping term, σ , drives the solution along the boundaries to the quiescent state, supporting the numerical solution. The introduction of these artificial terms imposes numerical forcing in the boundary region, which causes spurious waves back into the physical domain. To ease this problem, a smooth transition in compact support from the physical domain to $|U(x_1)| \geq c$ is required. Furthermore, the nonreflective efficacy of the buffer zone can be increased by increasing the size [37].

One of the strengths of Freund's method is that it can be applied to both the inflow and outflow boundaries. To eliminate the problem of unknown waves propagating inward at an outflow boundary, $U(x_1)$ is defined with an outward convective velocity above c . Now all of the characteristic waves propagate with a net outward velocity, so that the boundary behavior is fully described by the solution interior to the domain. Furthermore, $\sigma(x_1)$ serves to quickly dampen outgoing waves to prevent spurious reflections, which are caused by the numerical forcing induced by the addition of the artificial terms. Since $U(x_1)$ is directed outwards, nonphysical reflections propagating inward from the boundary are slowed, spending longer time in the dissipative boundary zone [11].

On an inflow boundary, $U(x_1)$ is chosen to be inward pointing. The effect of this is twofold. Structures and desired flow characteristics that are passed into the domain propagate quickly through the nonphysical boundary zone, undergoing minimal artificial damping. Additionally,

acoustic waves propagating upstream are asymptotically slowed and dissipated to the quiescent state [11].

2.3.5 Ffowcs-Williams Hawkins Analysis

While efficient computation favors a minimizing of the domain, the acoustic far-field and regions of interest can be quite large. In addition to spatial demands, direct computation of aeroacoustics concurrent with the flow field places heavy computational demands alongside the difficulty of accurately resolving acoustic radiation scales. To circumvent these difficulties, hybrid methods are used, where an appropriate acoustic analogy is solved after the flow solution is determined. The Ffowcs Williams Hawkins method has shown to be a popular approach. In theory, this amounts to solving the Ffowcs Williams Hawkins equation (2.25) upon a computationally derived flow solution. Practically, analysis of the Ffowcs Williams Hawkins equation (2.25) runs into several challenges.

In its exact form, it contains a computationally expensive volume integral of the stress tensor T_{ij} , which itself is expensive to compute. Furthermore, in two dimensions, the Green's function

$$G(\mathbf{x}, \mathbf{y}, t - \tau) = \frac{H(c_0(t - \tau) - |\mathbf{x} - \mathbf{y}|)}{2\pi c_0 \sqrt{c_0^2(t - \tau)^2 - |\mathbf{x} - \mathbf{y}|^2}} \quad (2.47)$$

necessitates a infinite time integral. While truncation of the time span can be used to approximate the solution, the timespan required could still pose computational difficulties [23].

An eloquent way around this is to perform the integration in the frequency domain. A flow solution only needs to be run long enough to arrive at a steady periodic solution. For aperiodic flows, windowing of the solution can be used to approximate a periodic state. Algorithms for both two and three dimensional Ffowc Williams Hawkins integrations in the frequency domain are readily available [23].

The presence of the volume integral can be approximated by appropriate placement of the Ffowcs Williams Hawkins surface S . While it is natural to consider a computational surface coinciding with the surface of solid obstacles in the flow, it is not required. Alternatively, a fully

permeable surface in the flow may be prescribed. Placement of such a surface precludes the ability to predict the radiation field within the surface, but since far-field acoustics are primarily considered, this limitation is of little practical consequence. Placement of S is determinant on the flow in question. The volume integral across the stress tensor is performed outside of S , so in choosing S to fully encompass all significant shear stresses, (2.25) can be sufficiently approximated even with neglecting the volume integration. Though the surface integrals do not explicitly consider the quadrupole source, shear mixing effects within S are captured by the monopole and dipole terms. Furthermore, quadrupole terms are less efficient than other sources, so eliminating the volume integral can be done safely except in extended quadrupole dominated fields. Flows, like free jets, where there are no strict monopole or dipole terms, and the quadrupole field extends semi-infinitely, become problematic with these methods [23].

Chapter 3

Parallelization of Ray-Tracing Algorithm and Aeroacoustic Analogy

3.1 Extension of CAD Model Analysis Algorithm to Parallel Computers

Geometry for complex obstacles can be efficiently generated using CAD software. In order to use the geometry with volume penalization methods, a masking function $\chi(\mathbf{x})$ for a given grid must be constructed from the CAD files. Tracing rays emitted from grid points, and counting their intersections with the obstacle surfaces, effectively determines the local χ value.

3.1.1 Optimization of Ray-Tracing for Structured, Multi-Resolution Grid

Incorporation of the ray tracing algorithm into the adaptive solver must be done carefully to preserve computational efficiency. For the ray-tracing algorithm that is used with the AWC solver, not all nodes incur equal computational cost. First, when the geometry is initialized, a bounding box is created reflecting the extents of the geometry on the cardinal axes. For external flow regimes, this efficiently determines χ for the large number of points that are not in the vicinity of the obstacle at a minimum cost.

At the next level, points that fall within the bounding box are considered. For rays parallel to the principle axes, root finding algorithms are used to determine the location of intersections. The computational cost is highly dependent upon the total number of intersections, the type of surface, and the nature of the geometry itself. This particular code classifies discrete geometry elements as either a revolved or non-uniform rational B-spline (NURBS) entity.

One practical difficulty with implementation of the algorithm is the representation of complex

geometry as a conglomeration of distinct entity. Contact surfaces between entities need to be rendered as internal points for the overall geometry. However, points on the surface can be rendered as external when the surface itself is counted as an intersection. When the grid adapts on the perceived surface, this causes the needless addition of large numbers of points along the internal seam between entities, as shown in Figure 3.1a. The geometry consists of a half-circle and half-ellipse joined along the minor axis. This effect is avoided by adding in a nominal offset smaller than the finest resolution of the grid. The discrete mask, χ , is unaffected, but the internal seam is removed, as in Figure 3.1b.

In general, each point with an intersecting ray will add appreciable computational cost to a calculation as the root-finding algorithms must converge to a precision that is smaller than the finest resolution of the grid. For large numbers of points, the relative computational cost can comprise a large portion of the computation time, especially if all nodes points must be re-evaluated at each time step.

In the case of the AWC, the structured nature of the grid can be a distinct advantage. For a fixed object, the masking function is static, so that the in/out data associated with any given point does not change for the duration of the calculation. Unique points only need to be evaluated once. Much of the computational load for geometry analysis is therefore shifted to the grid adaptation on initial conditions, and only new points in the grid evaluated thereafter. The largest contributions to computational cost then come from highly transient structures that cause grid adaptation in the immediate vicinity of the obstacle.

3.1.2 Ray-Tracing for Parallel Computing

Parallelization of the ray-tracing algorithm proceeds in a straightforward fashion. The masking function, χ , as well as an new-point identifier are attached to the point and communicated between processors as the solution is partitioned and repartitioned throughout the duration of a calculation. Once initialized, the geometry definitions are held in the memory, requiring only a single file I/O per processor. Though each point is evaluated independently, the parallelization

of the code is highly problem specific. Subdomains containing highly transient solutions in the vicinity of computationally intensive geometry will incur a high cost, while static structures away from the obstacle are only marginally impacted.

3.1.3 Results and Discussion

The computational load of the ray-tracing algorithm is considered for a two dimensional acoustic scattering problem. The geometry consists of a cylinder located at the origin on a computational domain of $\Omega = [-2, 3.5] \times [-2, 2]$, and asymmetric about the y-axis. The cylinder is elliptical for $x < 0$ and circular for $x > 0$. In the IGES format, it is represented by both recognized geometric entities: a revolved and a NURBS surfaces.

The propagation and scattering of an acoustic wave from a source at $x = 2$ causes the grid to adapt continually for the duration of the calculation. The grid adapts in all regions of Ω , including in the immediate vicinity of the obstacle. Though simple, this problem represents the broad spectra of difficulties for effective code parallization.

Figure 3.2 shows the total CPU time for the CAD analysis calculations at each timestep vis-à-vis the total number of grid points. A majority of the total walltime is incurred during the initializing of the grid. For the first several hundred iterations in time, the grid adapts heavily as the acoustic perturbation begins to propagate outward. However, since the points added are far away from the obstacle, the root finding algorithms are not used and the computational cost is negligible. When the acoustic waves approach the obstacle, near iteration 7000, ray-tracing is necessary to determine the mask for each point, and the computational cost rises accordingly. However, the number of points analyzed remains small.

The strong scaling for the ray-tracing algorithms in Figure 3.3 shows the embarrassingly parallel nature of this method for the problem considered.

3.2 Parallel Implementation of Ffowcs-Williams Hawkings Integration Surface

In order to calculate the aeroacoustic far-field, the time-accurate flow solution is needed for the Ffowcs Williams and Hawkings equations. The FWH code, developed by Lockard [23], requires constant time stepping and static nodes for the flow variables on the integration surface. Since aeroacoustic analysis is performed in post-processing, interfacing with the AWCM code only demands that appropriate solution files are produced and a strictly defined integration surface imposed in the computational grid.

3.2.1 Review of Serial Interface

The FWH code has previously been used with the AWCM code for serial cases, and the interface is quite direct. The surface of integration for the FWH equations is defined by a discrete number of linear patches that are parallel to the principle axes. They are generated during the initialization of the code by adding points to the adaptive grid at a desired level of resolution. The most efficient patches have endpoints that lie on the j_{\min} grid level to avoid unnecessary adaptation. Once constructed, the variables are simply written at desired timesteps.

3.2.2 FWH parallel Interface

The parallel implementation of the FWH interfacing minimally affects the construction of the integration surface. During initialization, the FWH surface is defined on all processors, and each processor filters out points not resident to the local subdomain at each time step. At the desired timestep, all information for FWH points are passed to processor 0 for writing. In cases where it would be desirable to use an adaptive timestep, the parallel overhead is greater. Communication is required at every iteration in order to retain the integration surface in memory for interpolation.

3.2.3 Results and Discussion

Strong scaling is examined for two-dimensional acoustic scattering from an arbitrary solid obstacle located at the origin. The FWH surface is constructed so that it resides on multiple processors. A simple, first-order interpolation is used here for an adaptive, though higher-order schemes may be used with no additional communication requirements. The strong scaling for writing of FWH information is shown in Figure 3.4. The speedup is slightly less than 1, however, the adaptive timestep is a worst case scenario and the low relative computational overhead makes this approach a feasible option.

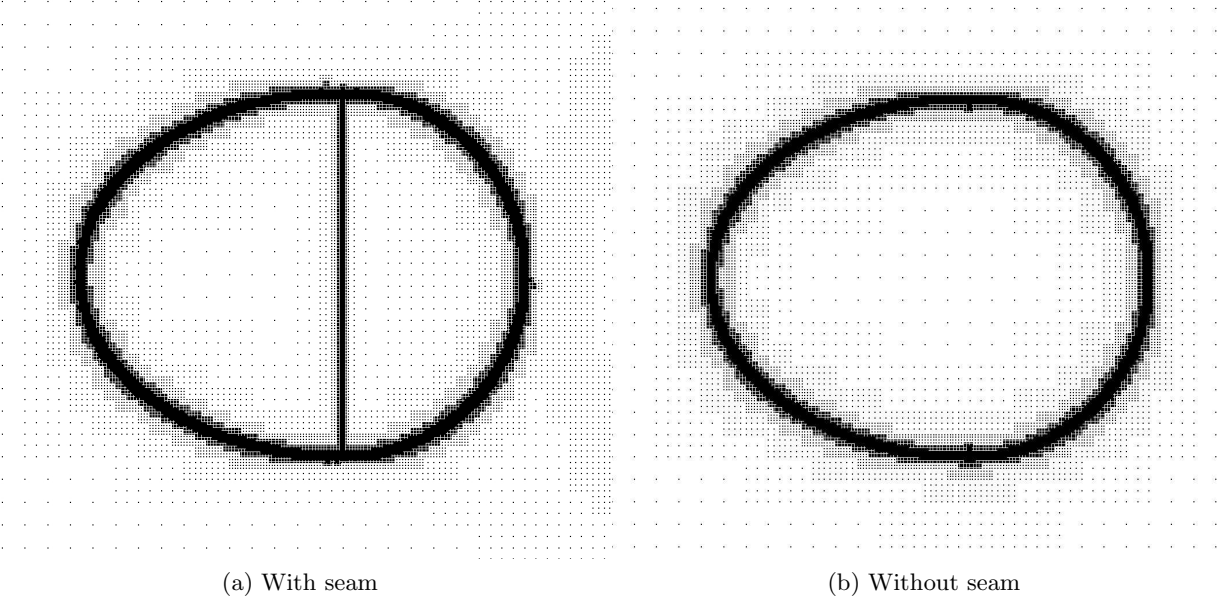


Figure 3.1: Grid adapted to solid obstacle comprised of elliptical and circular entities.

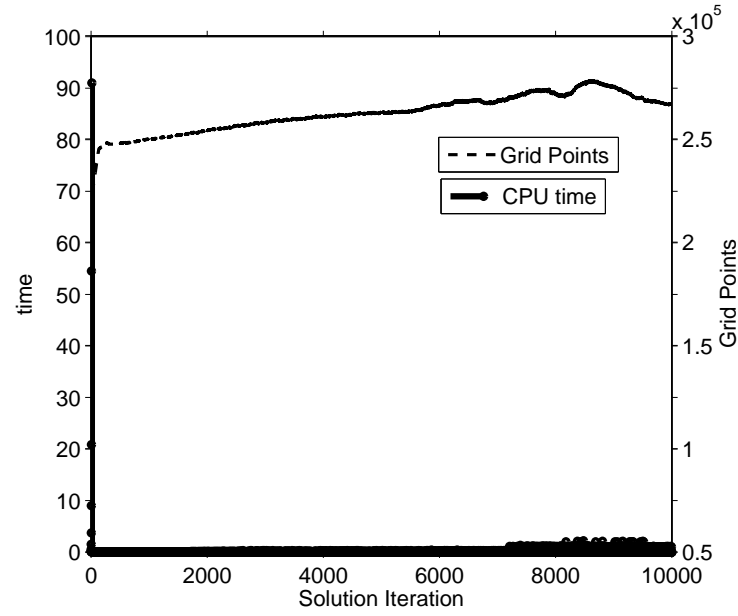


Figure 3.2: CPU time of CAD analysis and number of grid points at every timestep.

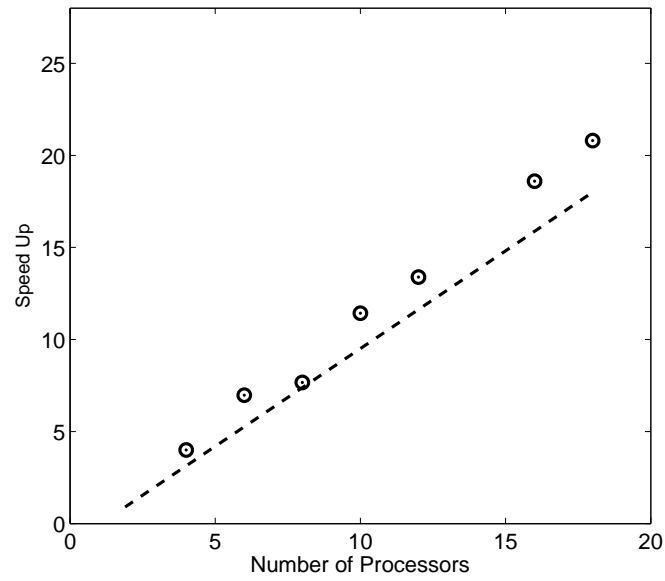


Figure 3.3: Strong scaling of CAD algorithm.

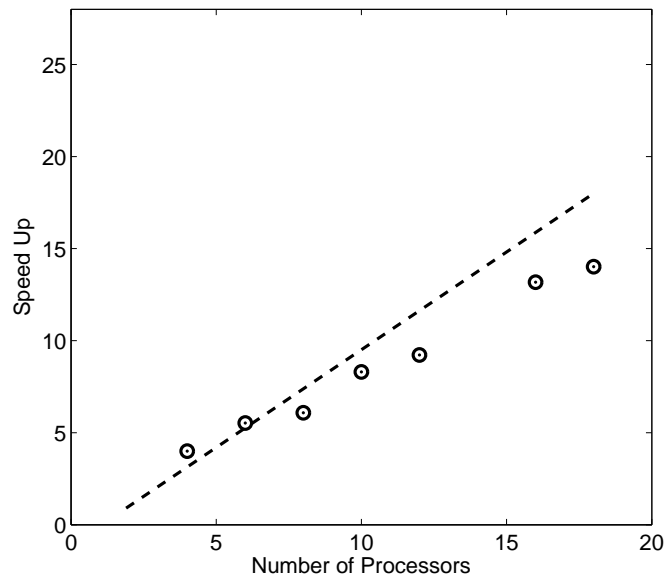


Figure 3.4: Strong scaling for writing of FWH integration surface to file.

Chapter 4

Characteristic-Based Volume Penalization Method

Immersed boundary methods have been developed to model flows around a solid obstacle without the need for body conformal meshes. While pseudo-conformal and multi-resolution grids are often used [2, 13, 7, 21], releasing the requirement for node/surface coincidence allows one to avoid costly re-meshing. This proposed method builds upon some of the principles that are employed for the Brinkman Penalization Method for compressible flows [21], particularly the treatment of Dirichlet boundary conditions.

While Brinkman penalization has shown to be effective in many fluid applications [2, 21], the drawbacks are pronounced. Steep gradients at the surface have shown to be problematic, requiring diffuse boundaries or, for Bae and Moon, local changes in differencing stencil [2]. Brinkman penalization is also limited to a small set of fluid problems and lacks generalizability.

The premise of this new Characteristic-Based Volume Penalization (CBVP) is to use Brinkman-style forcing for Dirichlet conditions, while introducing penalized convective terms to impose Neumann conditions. For Neumann conditions, the dominant penalization terms force the equations into a hyperbolic system with a single, inward-pointing characteristic. That way, the nonphysical penalized region only affects the physical solution through the derivative values at the boundary.

4.1 Characteristic-Based Volume Penalization

Characteristic-Based Volume Penalization allows for the implementation of Dirichlet, Neumann, and Robin type boundary conditions by introducing forcing into the constitutive equations.

For a domain, Ω containing obstacles O_i , desired boundary conditions are to be imposed upon the obstacle surfaces S_i . Penalization is applied only to the region inside of the obstacle by mean of a masking function, χ , where

$$\chi = \begin{cases} 1 & \text{if } \mathbf{x} \in O_i, \\ 0 & \text{otherwise.} \end{cases}$$

The expression of penalized terms, and therefore the strict enforcement of the boundary conditions, is controlled by penalization parameter, η , in such a way that the solution converges as $\eta \rightarrow 0$.

Dirichlet conditions are imposed in the same fashion as with the Brinkman penalization method [21]. For a generalized quantity, the penalization term is added to the constitutive equation to provide forcing toward some target value, U_0 , by

$$\frac{\partial u}{\partial t} = \dots \text{RHS} \dots - \frac{\chi}{\eta_b}(u - U_0), \quad (4.1)$$

where $\partial u / \partial t$ is a general constitutive equation for some variable of interest.

Neumann boundary conditions can be imposed by introducing similar-style forcing on the normal derivative. For a target normal derivative q the governing equation for u is penalized

$$\frac{\partial u}{\partial t} = \dots \text{RHS} \dots - \frac{\chi}{\eta_c} n_k \left(\frac{\partial u}{\partial x_k} - q \right), \quad (4.2)$$

for a desired value, q , where $n_k \hat{e}_k$ is the inward pointing surface normal of the obstacle. As η_c becomes small, the penalization term begins to dominate (4.2). While the right hand side of the constitutive equation is still present in the penalized region, it acts on a much larger timescale. For a sufficiently small penalization parameter, (4.2) becomes a hyperbolic equation,

$$\frac{\partial u}{\partial t} = -\frac{\chi}{\eta_c} n_k \left(\frac{\partial u}{\partial x_k} - q \right) \quad (4.3)$$

within the obstacle. For (4.3), there is a single characteristic pointing inward on the obstacle, and the steady state solution is

$$\frac{\partial u}{\partial x_k} = q. \quad (4.4)$$

The solution u on s_i is governed by the constitutive equations, while the nonphysical internal region only affects the fluid through the normal derivative. The characteristic ensures that the nonphysical internal solution does not propagate outward.

Note that these schemes (4.1-4.2) are generic and not applied to any particular system of PDE's. Penalization can be independently imposed for any set of problem specific quantities, and extended to the governing system provided that consistent relationships are available.

4.1.1 Penalized Navier-Stokes Equations

For the problems considered here, penalization is prescribed for adiabatic, zero mass-flux, and no-slip boundary conditions on immersed boundaries S_i . That is

$$\left. \begin{aligned} \frac{\partial \rho}{\partial n} &= 0, \\ \mathbf{u} &= \mathbf{U}_0, \\ \frac{\partial T}{\partial n} &= 0, \end{aligned} \right\} \text{ on } S_i \quad (4.5)$$

must be satisfied. While the zero-flux condition is disingenuous considering the adiabatic condition, it is an approximation made to simplify and speed up the calculation. The approximation comes from boundary conditions for the Euler equations, where the lack of viscous stress gives a pressure gradient of zero.

To enforce this set of boundary conditions, equations are assumed of the form

$$\frac{\partial \rho}{\partial t} = \dots - \frac{\chi}{\eta_c} n_k \frac{\partial \rho}{\partial x_k}, \quad (4.6)$$

$$\frac{\partial \rho u_i}{\partial t} = \dots - \frac{\chi}{\eta_b} \rho (u_i - U_{0i}), \quad (4.7)$$

$$\frac{\partial T}{\partial t} = \dots - \frac{\chi}{\eta_c} n_k \frac{\partial T}{\partial x_k}. \quad (4.8)$$

Note that both (4.6) and (4.8) make use of the same parameter, η_c . This is following a simplest convention of penalizing like conditions similarly. Using (4.6-4.8), the ideal gas equation, and the energy equation of state, the penalized nondimensional Navier-Stokes equations for boundary

conditions (4.5) are

$$\frac{\partial \rho^*}{\partial t^*} = -\frac{\partial \rho^* u_j^*}{\partial x_j^*} \boxed{-\frac{\chi}{\eta_c} n_k \frac{\partial \rho^*}{\partial x_k^*}}, \quad (4.9)$$

$$\frac{\partial \rho^* u_i^*}{\partial t^*} = -\frac{\partial(\rho^* u_i^* u_j^*)}{\partial x_j^*} - \frac{\partial p^*}{\partial x_i^*} + \frac{1}{Re_a} \frac{\partial \tau_{ij}^*}{\partial x_j^*} \boxed{-\frac{\chi}{\eta_b} \rho^* (u_i^* - U_{0i}^*)}, \quad (4.10)$$

$$\begin{aligned} \frac{\partial \rho^* e^*}{\partial t^*} = & -\frac{\partial}{\partial x_j^*} [(\rho^* e^* + p^*) u_j^*] + \frac{1}{Re_a} \frac{\partial(u_i^* \tau_{ij}^*)}{\partial x_j^*} + \frac{1}{(\gamma-1)} \frac{1}{Re_a Pr} \frac{\partial}{\partial x_j^*} \left(\mu \frac{\partial T^*}{\partial x_j^*} \right) \\ & \boxed{-\frac{\chi}{\eta_c} \frac{1}{(\gamma-1)} n_k \frac{\partial p^*}{\partial x_k^*} - \frac{\chi}{\eta_b} \rho^* u_i^* (u_i^* - U_{0i}^*) + \frac{\chi}{\eta_c} \frac{u_i^* u_i^*}{2} n_k \frac{\partial \rho^*}{\partial x_k^*}}, \end{aligned} \quad (4.11)$$

where it remains unchanged that

$$\begin{aligned} p^* &= \frac{\rho^* T^*}{\gamma}, \\ \tau_{ij}^* &= \mu^* \left(\frac{\partial u_i^*}{\partial x_j^*} + \frac{\partial u_j^*}{\partial x_i^*} - \frac{2}{3} \frac{\partial u_k^*}{\partial x_k^*} \delta_{ij} \right), \\ e^* &= \frac{1}{2} u_i^* u_i^* + c_p T^* - \frac{p^*}{\rho^*}. \end{aligned}$$

In a general sense, equations (4.9-4.11) are valid on all Ω . However, strict application across the domain can lead to a convergence of characteristics with multi-valued singularities. This will invariable arise for any geometry where the surface normals converge within the computational domain, such as the typical case of a fully enclosed obstacle. Depending on the variables penalized in this manner, this can lead to accumulation in the regions of intersection. However, the region where the penalization terms affect the fluid solution is limited to a narrow region along the inside surface of the obstacle. For the adaptive wavelet solver used here, this region only consists of the points belonging to the differencing stencil for any fluid node. By properly resolving the obstacle, intersections can typically be avoided, except in the case of thin geometry. The penalization in (4.2) therefore only has local support within this narrow region, and effective sink terms prevent accumulations within the obstacle. Distance functions based on the masking term χ have been used effectively to provid local support functions, though their practical construction is omitted here.

4.2 Stability and Artificial Viscosity

As noted by Liu and Vasilyev, the Brinkman term, η_b , introduces additional stiffness into the problem [21]. The solution in $\rho \mathbf{u}$ evolves on the timescale of η_b within the obstacle. At the interface, this forcing creates high-frequency transient structures that propagate outward into the fluid domain. These structures are of the length-scale $\delta = \sqrt{\frac{\eta_b}{Re_a}}$. For stability, these structures ought to be resolved, implying a mesh resolution of $\Delta x_i < \sqrt{\frac{\eta_b}{Re_a}}$ at every resolution on the adaptive grid. For moderate values of η_b , the resolution requirements can quickly become computationally burdensome, even for adaptive multi-resolution methods.

One solution would be to use a diffuse boundary region for the obstacle, where χ transitions smoothly from 1 to 0 across a finite distance. Since a sharp interface becomes important at high Reynolds numbers, an alternative method is to use artificial viscosity to dampen these high frequency structures at the solid-fluid interface. The length scale δ associated with viscous damping ν on timescale τ is $\delta^2 = \nu\tau$; so for a prescribed resolution, the artificial viscosity ν_n required to dampen η_b timescale structures is

$$\nu_n > \frac{\Delta x^2}{\eta_b}. \quad (4.12)$$

That is to say that ν_n , the necessary viscosity for numerical stability, is dependant upon the desired resolution. For low Reynolds number flows or high resolution grids, this requirement will be met by the physical viscosity. Where this requirement is not met, artificial viscosity can be provided to compliment the physical viscosity through

$$\nu_n = \max \left\{ \alpha \frac{\Delta x^2}{\eta_b} - \frac{1}{Re_a}, 0 \right\}, \quad (4.13)$$

where α is a factor of $O(1)$. This viscosity is needed only in a narrow region outside the interface to dampen the acoustic structures as they propagate outward into the fluid. The timescale of acoustic propagation through the viscous zone δ_ν is $\tau = \delta_\nu/c$, and the zone itself must be sufficiently resolved, $\Delta x < \delta_\nu$. Therefore, the width of the zone with viscosity given by (4.12) must be

$$\delta_\nu = O\left(\frac{\eta_b}{\alpha}\right). \quad (4.14)$$

For a given spatial resolution, the strength of the artificial viscosity increases on $O(\frac{1}{\eta_b})$, while the thickness of this zone decreases on $O(\eta_b)$ as stronger penalized forcing implies higher frequencies. The practical lower limit of the viscous zone is determined by the grid spacing, $\delta_\nu = \Delta x$. In this case the effect is solely in increased viscosity without corresponding reduction of the zone width. Therefore, where the penalization is not sufficiently resolved, there is a lower effective limit of η_b , beyond which there is no further reduction in error. As η_b goes to 0 at a specified resolution, the higher artificial viscosity begins to contribute significantly to the error of the solution.

4.3 Error Estimation From Acoustic Theory

The addition of the convective terms associated with penalization parameter η_c on the Navier-Stokes equations, (4.9-4.11), implies a discontinuous change in the speed of sound at the interface. From acoustic theory, this impedance mismatch would cause physical reflection of incoming waves based upon the relation. The reflection coefficient for incident pressure waves at an interface is

$$R = \frac{Z_2 - Z_1}{Z_2 + Z_1}, \quad (4.15)$$

where the impedance in terms of the density, cross-sectional area S , and speed of sound c is $Z = \rho c/S$. Since the density and cross-sectional area of the fluid for both regions is equal at the boundary, R is simply given by

$$R = \frac{c_2 - c_1}{c_2 + c_1} = \frac{1 - \eta_c}{1 + \eta_c} \approx 1 - 2\eta_c. \quad (4.16)$$

For reflected acoustic waves, the expected amplitude error is $O(\eta_c)$. However, it is worthwhile to note that does not consider the errors introduced from the penalized no-slip condition.

4.4 Asymptotic Analysis

While the penalized Navier-Stokes equations cannot be directly analyzed, rigorous asymptotic analysis of the acoustic timescale behavior gives insight into the error convergence of the penalization parameters η_b and η_c . One-dimensional flow is considered for an acoustic pulse reflecting off an obstacle. The error is examined in the fully reflected pulse.

For simplicity, a further modification is made to the penalized Navier-Stokes equations (4.9-4.11). The inviscid (Euler equation) terms are removed within the penalized region.

$$\frac{\partial \rho^*}{\partial t^*} = -\boxed{(1-\chi)} \frac{\partial \rho^* u_j^*}{\partial x_j^*} - \frac{\chi}{\eta_c} n_k \frac{\partial \rho^*}{\partial x_k^*}, \quad (4.17)$$

$$\frac{\partial \rho^* u_i^*}{\partial t^*} = -\boxed{(1-\chi)} \left[\frac{\partial(\rho^* u_i^* u_j^*)}{\partial x_j^*} + \frac{\partial p^*}{\partial x_i^*} \right] + \frac{1}{Re_a} \frac{\partial \tau_{ij}^*}{\partial x_j^*} - \frac{\chi}{\eta_b} \rho^* (u_i^* - U_{0i}^*), \quad (4.18)$$

$$\begin{aligned} \frac{\partial \rho^* e^*}{\partial t^*} = & -\boxed{(1-\chi)} \frac{\partial}{\partial x_j^*} [(\rho^* e^* + p^*) u_j^*] + \frac{1}{Re_a} \frac{\partial(u_i^* \tau_{ij}^*)}{\partial x_j^*} + \frac{1}{(\gamma-1)} \frac{1}{Re_a Pr} \frac{\partial}{\partial x_j^*} \left(\mu \frac{\partial T^*}{\partial x_j^*} \right) \\ & - \frac{\chi}{\eta_c} \frac{1}{(\gamma-1)} n_k \frac{\partial p^*}{\partial x_k^*} - \frac{\chi}{\eta_b} \rho^* u_i^* (u_i^* - U_{0i}^*) + \frac{\chi}{\eta_c} \frac{u_i^* u_i^*}{2} n_k \frac{\partial \rho^*}{\partial x_k^*}. \end{aligned} \quad (4.19)$$

It is important to retain the viscous terms everywhere on Ω for stability. Removing viscous terms would create a discontinuity from the Brinkman penalization for Dirichlet condition (4.1).

4.4.1 Asymptotic Analysis of the Fluid Region

First the case is considered where $\eta_c \ll \eta_b$. It will be shown that the asymptotic expansions of (4.17-4.19) for this case are of the same form and indicate the same order of error as when $\eta_c \ll \eta_b$ or $\eta_c = \eta_b$. For the region occupied by the fluid, the leading perturbation terms for nondimensionalized flow variables are

$$\rho_f(x, t) = 1 + \epsilon \rho'_{0f} + \epsilon \eta_b \rho'_{1f} + \dots, \quad u_f(x, t) = \epsilon u'_{0f} + \epsilon \eta_b u'_{1f} + \dots, \quad (4.20)$$

$$p_f(x, t) = \frac{1}{\gamma} + \epsilon p'_{0f} + \epsilon \eta_b p'_{1f} + \dots, \quad T_f(x, t) = 1 + \epsilon T'_{0f} + \epsilon \eta_b T'_{1f} + \dots \quad (4.21)$$

Substitution into (4.17-4.19) and retaining only first order terms yields the linear system

$$\frac{\partial u'_f}{\partial t} + \frac{\partial p'_f}{\partial x} = 0, \quad (4.22)$$

$$\frac{\partial p'_f}{\partial t} + \frac{\partial u'_f}{\partial x} = 0, \quad (4.23)$$

for both zero- and first-order perturbation quantities. Viscous terms are neglected in the high Reynolds number limit, where $\frac{1}{Re} \ll \eta_b$. Additionally, the relation $\rho'_f = p'_f$ holds, and the flow is isentropic. The resulting system (4.22-4.23) is simply the linear acoustic equations, describing small amplitude pulses propagating through the fluid.

4.4.2 Asymptotic Analysis of the Penalized Region

Within the penalized region, representative of a solid obstacle, the asymptotic expansion of flow variables differs from the fluid region in the zero-order velocity term. The effect of the Brinkman penalization term on the momentum equation is to dampen the velocity to near-zero quantities. Once again, considering the case where $\eta_c \ll \eta_b$, the flow variables through the first-order perturbations is

$$\rho_p(x, t) = 1 + \epsilon \rho'_{0p} + \epsilon \eta_b \rho'_{1p} + \dots, \quad u_p(x, t) = \epsilon \eta_b u'_{1p} + \dots, \quad (4.24)$$

$$p_p(x, t) = \frac{1}{\gamma} + \epsilon p'_{0p} + \epsilon \eta_b p'_{1p} + \dots, \quad T_p(x, t) = 1 + \epsilon T'_{0p} + \epsilon \eta_b T'_{1p} + \dots \quad (4.25)$$

Retaining first-order terms from (4.17-4.19) gives the following system in terms of the first-order perturbation quantities,

$$\frac{\partial \rho'_p}{\partial t} + \frac{1}{\eta_c} \frac{\partial \rho'_p}{\partial n} = 0, \quad (4.26)$$

$$\frac{\partial u'_p}{\partial t} + \frac{1}{\eta_b} u'_p = 0, \quad (4.27)$$

$$\frac{\partial p'_p}{\partial t} + \frac{1}{\eta_c} \frac{\partial p'_p}{\partial n} = 0, \quad (4.28)$$

where n indicates the inward-pointing normal. Again, the isentropic relation $\rho'_f = p'_f$ holds. Here, the decision to remove inviscid terms from the Navier-Stokes equations is justified, as the equations are completely uncoupled within the penalized region, and as such, the analytical solution is much more straightforward.

The perturbation equations (4.26-4.28) form a linear hyperbolic system of PDEs with a single characteristic pointing inward on the penalized domain. Strong damping on velocity drives the solution towards the no-slip condition. In order to ensure continuity within the penalized domain, viscous terms from (4.18) must be retained. Assuming constant viscosity, (4.27) becomes

$$\frac{\partial u'_p}{\partial t} + \frac{1}{\eta_b} u'_p - \frac{1}{Re} \frac{\partial^2 u'_p}{\partial x^2} = 0. \quad (4.29)$$

4.4.3 Asymptotic Analysis of Error Convergence

In order to examine the error convergence as $\eta_b, \eta_c \rightarrow 0$, the two systems (4.22-4.23) and (4.26-4.28) are solved on a one-dimensional split domain. Fluid occupies the semi-infinite region $x < 0$, while $x \geq 0$ is considered the solid obstacle and appropriately penalized.

The solution in the fluid region, in terms of initial $(u'_0(x), p'_0(x))$ conditions and boundary values $(u'_1(t), p'_1(t))$ at the fluid-obstacle interface, is

$$u'_f(x, t) = \frac{1}{2}u'_0(x-t) + \frac{1}{2}p'_0(x-t) + \frac{1}{2}u'_1(x+t) - \frac{1}{2}p'_1(x+t) \quad (4.30)$$

$$p'_f(x, t) = \frac{1}{2}u'_0(x-t) + \frac{1}{2}p'_0(x-t) - \frac{1}{2}u'_1(x+t) + \frac{1}{2}p'_1(x+t) \quad (4.31)$$

for both zero- and first-order perturbations.

The solution in the penalized region can be determined for each variable independently. The first order perturbation of pressure is easily solved based on the propagation of boundary conditions for a single characteristic with speed $\lambda = \frac{1}{\eta_c}$,

$$p'_p(x, t) = p'_1(t - \eta_c x). \quad (4.32)$$

The first order velocity perturbation of u'_p can be solved by transforming (4.29) into the form of an inhomogeneous heat equation through

$$w(x, t) = e^{-\frac{t}{\eta_b}}(u'(x, t) - u'(0, t)). \quad (4.33)$$

With continuity of the first derivative implied with the fluid domain, the solution of $u'(x, t)$ on the semi-infinite domain is known [4]. Provided that the limits of the solution are finite and constant as $x \rightarrow 0$ for variable parameter η_b , then the solution at the interface, $u^*(t) = u'_p|_{x=0}$, is $O(\eta_b)$. Now considering the timescale $t \gg \eta_b$, the quasi-steady state solution to the boundary value problem (4.29) is found to be

$$u'_p(x, t) = u^*(t) \exp\left(-x \frac{Re_a}{\eta_b}^{1/2}\right). \quad (4.34)$$

Enforcing continuity and smoothness between the fluid domain and penalized domain solutions, $u'_f|_{x=0} = u'_p|_{x=0}$ and $\frac{\partial u'_f}{\partial x}|_{x=0} = \frac{\partial u'_p}{\partial x}|_{x=0}$, yields the acoustic solution with leading error terms $O(\eta_c, \eta_b^{1/2})$.

4.5 Results and Discussion

The first benchmark problem is to verify the behavior of penalized equations for each of the Dirichlet and Neumann boundary conditions. One dimensional heat conduction transients allow for each boundary condition to be examined in the simplest case of a scalar valued solution without the effects of coupling.

Two general groups of fluid benchmark problems are considered to validate the penalization for no-slip, adiabatic boundary conditions on coupled equations. The first group is for acoustic scattering problems, and directly corresponds to the asymptotic analysis earlier in this chapter. A one dimensional case is used to show convergence of the solution on the penalization parameters. A second case shows a multi-dimensional application and the validity of curved boundaries. The second group of fluid simulations is formed around the canonical problem of external nonzero mean flow past a cylinder. Low Reynolds number, incompressible flow is used to validate the methods, especially for boundary layer separation, under the presence of a stabilizing viscous zone at the surface. Periodic vortex shedding is also considered to validate the methods for compressible flows at moderate Reynolds numbers.

All problems are solved using Freund-type boundary conditions in a zone bounding the physical domain. The characteristic length for two dimensional problems is the diameter of the cylinder.

4.5.1 Benchmark Problem I: One Dimensional Heat Conduction

Heat conduction provides a good platform for examining CBVP of each boundary condition individually. There is a corresponding physical application for each boundary condition, and furthermore, these problems exemplify the versatility of the method. Unlike earlier Brinkman methods, CBVP is not limited to fluid problems, but is rather a general form of individual boundary conditions that can be applied to a wide variety of PDEs.

The constitutive equation is the one-dimensional heat equation for nondimensional temper-

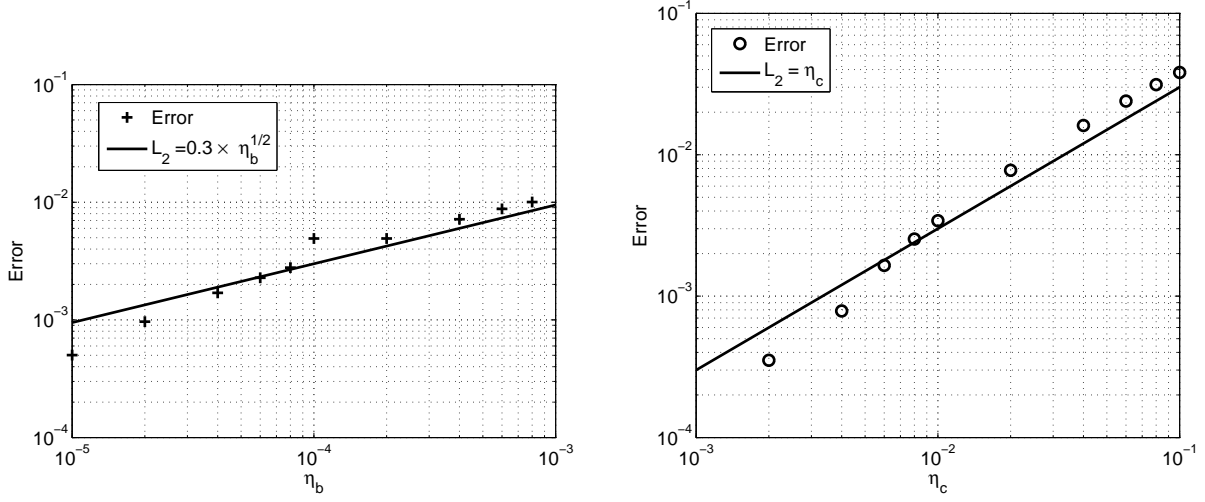


Figure 4.1: Time-averaged L_2 norm error for converging η_c and η_b .

ature perturbation T ,

$$\frac{\partial T}{\partial t} - k \frac{\partial^2 T}{\partial x^2} = 0, \quad (4.35)$$

and is applied in the physical domain. The physical domain consists of $\Omega = [-1, 0]$, while the penalized domain is $\Omega_p = [0, 0.5]$. For all cases, the initial conditions are $T_0(-1) = 1$ and $T_0(x) = 0$ elsewhere. The left boundary condition is $T(0, t) = 1$.

This problem is solved for a nonadaptive grid. In determining the error, the solution is compared with numerical results for the exact boundary conditions imposed in the usual fashion at the right physical boundary, $x = 0$. The resolution used for all simulations is $\Delta x = \frac{1}{1024}$. Errors are examined during the transient solution for a thermal conductivity of $k = 0.5$.

Penalization for the Dirichlet condition is prescribed by (4.1) for constant temperature $T(0, t) = 0$. In Figure 4.1a, the error can clearly be seen converging on $O(\eta_b^{1/2})$. This agrees with the expected error term introduced by the no-slip condition on the asymptotic analysis.

The Neumann condition for an adiabatic boundary, $\frac{\partial T}{\partial t} = 0$, is imposed by penalization of the form in (4.2). The error converges on $O(\eta_c)$, shown in Figure 4.1b, and agrees with the error introduced by the Neumann boundary condition from the asymptotic analysis.

4.5.2 Benchmark Problem II: One Dimensional Normal Wave

The penalized equations are solved on a domain $\Omega = [-0.5 \ 0.5]$, where the fluid occupies $\Omega_f = [-0.5 \ 0]$, and the solid obstacle is $\Omega_s = [0 \ 0.5]$. Initial conditions for the incident wave are given by Gaussian distributions in the perturbation quantities

$$\rho' = u' = 10^{-3} \exp \left[-\ln(2) \left(\frac{(x + 0.25)^2}{0.004} \right) \right], \quad (4.36)$$

with

$$e = \frac{1}{2} u_i u_i + c_p T - \frac{p}{\rho}. \quad (4.37)$$

The Reynolds number is $Re_a = 10^{-5}$.

This problem is first solved for the penalization scheme in (4.17-4.19) where the inviscid fluxes are removed and the penalized obstacle becomes uncoupled for $Re \rightarrow \infty$. This simplification corresponds to the equations used in the asymptotic analysis outlined in the previous section, and therefore error convergence of $O(\eta_c, \eta_b^{1/2})$ is expected. In the second set, where the Navier-Stokes equations are left intact within Ω_p , the problem is considered for both high-resolution cases where the stability requirement (4.12) is met, and a computationally efficient resolution where localized numerical viscosity is introduced.

Figure 4.2 shows a fully reflected wave for high resolution and artificial viscosity cases. Note the increased phase and amplitude errors introduced by the presence of the viscous layer for waves travelling in the negative x -direction. The more pronounced phase error arises from the increased offset stagnation point from the solid interface.

Where $\eta_b = 10^{-3}$, the highest effective resolution on the adaptive grid is $\Delta x = O(10^{-6})$, enough to resolve transient structures created by the Brinkman forcing term. For comparison, sufficient resolution of the boundary layer is $O(\frac{1}{\sqrt{Re_a}})$, or $O(10^{-3})$.

Figure 4.3a show the error convergence on a fully reflected pulse for the cases where $\eta_b = \eta_c$ and $\eta_b \gg \eta_c = 8 \times 10^{-4}$. The error convergence of both cases is the same, namely $O(\eta_b^{1/2})$, implying that the error introduced η_c is relatively lower than that of η_b . This result matches well to the asymptotic analysis presented in the previous section. For $\eta_c \gg \eta_b = 4 \times 10^{-5}$, the error was

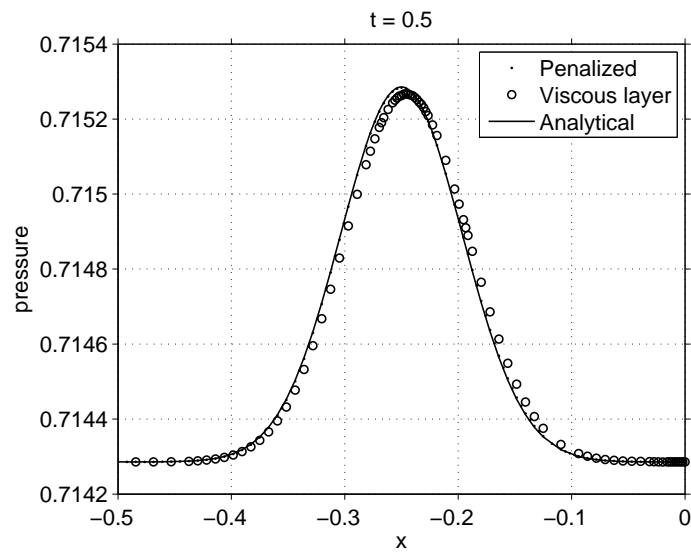


Figure 4.2: Fully reflected pressure waves for a high resolution penalized case, a case with artificial viscosity added near the solid interface, and the analytical solution.

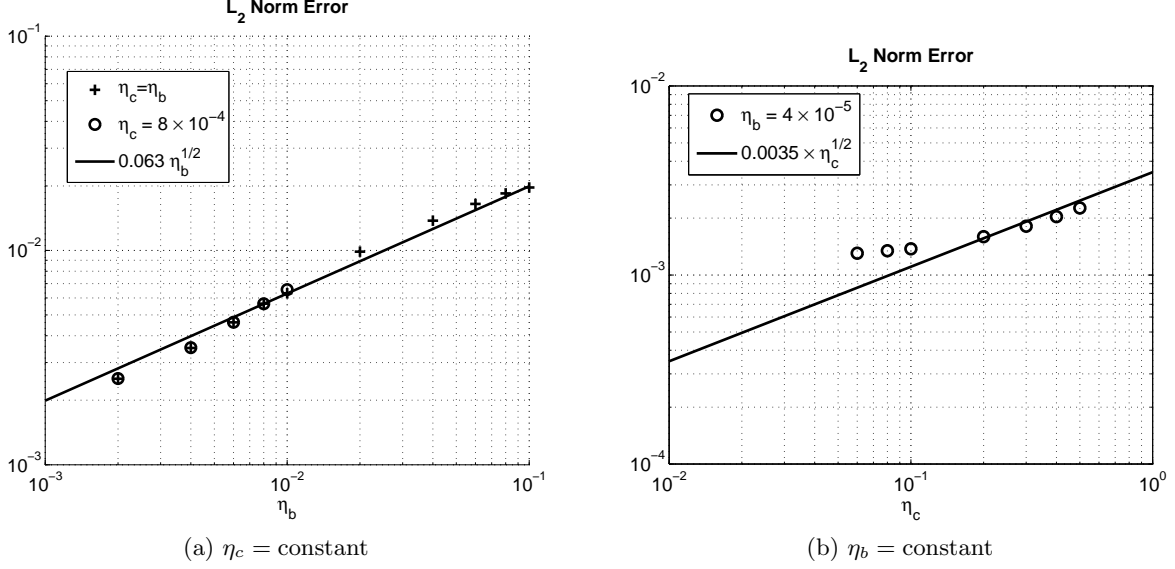


Figure 4.3: Time-averaged L_2 norm error for converging η_c and η_b with Euler terms removed.

examined for a pulse in mid reflection, and the L_2 norm error convergence shown in Figure 4.3b. The error converges on $\eta_c^{1/2}$ before quickly saturating from numerical viscosity. Note the disparate magnitudes of error incurred for cases where $\eta_b \cong \eta_c$. The value of η_b must be several orders of magnitude smaller than η_c in order to introduce comparable errors.

This result is beneficial for computational efficiency. When using Krylov-space time integration, the penalized equations have been found to be unstable in for η_c -based CFL that is much larger than $O(20)$. Satisfactory accuracy can still be obtained for $\eta_c = 0.1$, which allows for use of the acoustic CFL without implementing split timesteps.

The same problem was solved with the full Navier-Stokes equations left intact within the penalized region. Thus the equations remain coupled throughout the entire domain, even in the inviscid limit.

For $\eta_c = \text{constant}$, Figure 4.4a shows error convergence on $O(\eta_b)$. Conversely, where $\eta_b = \text{constant}$, Figure 4.4b shows initial error convergence on $O(\eta_c^{0.85})$, before saturating on some unknown error source. The translation in convergence plots for $\eta_c = \text{constant}$ and $\eta_b = \text{constant}$, in Figures 4.4a and 4.4b respectively, indicate general error convergence on $O(\eta_b(\eta_c + E)^{0.85})$, where E is the undetermined error term from Figure 4.4b. Again, we see that η_b ought to be the more

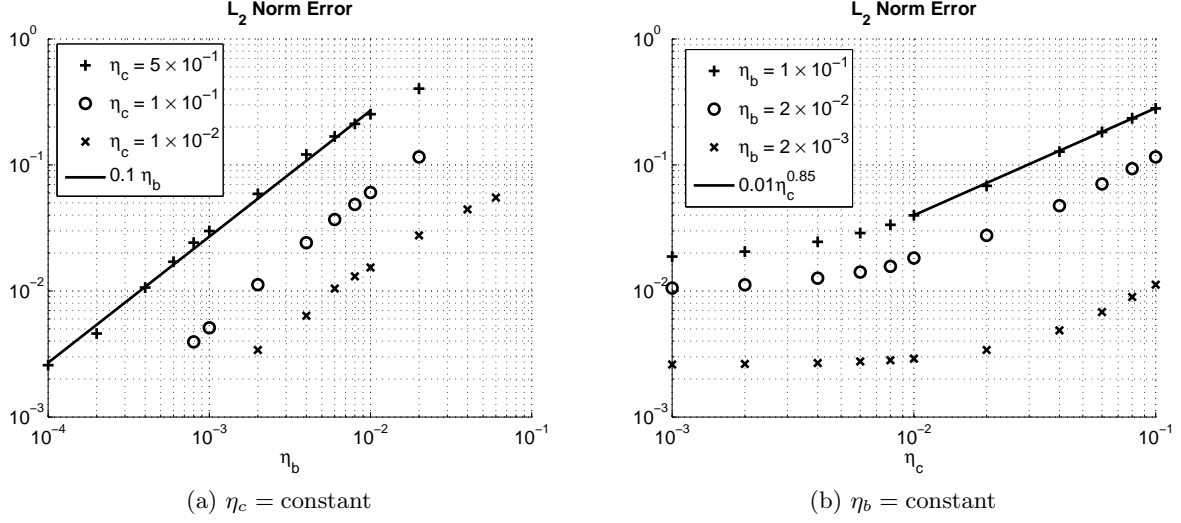


Figure 4.4: Time-averaged L_2 norm error for converging η_c and η_b .

strictly controlled parameter.

For lower resolution cases, where the viscosity requirement in (4.12) is not met, artificial viscosity was added to a narrow region in the vicinity of the solid interface. While the theoretical thickness of the viscous layer must be on $O(\eta_b)$, the practical implementation is much thicker. A smooth support function is desired to avoid discontinuities in the solution derivative. In order to properly resolve the diffuse boundary between the physical viscosity and the artificial viscosity, the zone is about three times thicker than the theoretical requirement.

With use of artificial viscosity, the error quickly saturates for a given resolution, as shown in Figure (4.5). Further convergence of η_b increases the viscosity requirement, and any accuracy gains are offset. Therefore, in such cases, the accuracy is controlled by the resolution.

4.5.3 Benchmark Problem III: Acoustic Scattering of a Single Source

Acoustic scattering from a two-dimensional cylinder is considered. This problem demonstrates multidimensional application of the penalization method, where the surface normal is different from the incidence angle of reflected waves. Furthermore, it shows the ability to resolve and properly model the effects of a curved surface. A cylinder of $r = 0.5$ is located at the origin, and

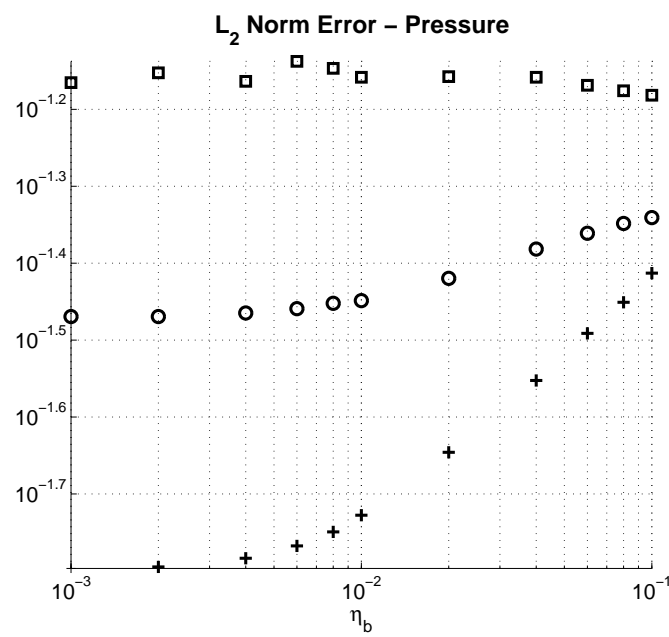


Figure 4.5: Error convergence for 1D acoustic reflection with artificial viscosity introduced at the solid interface.

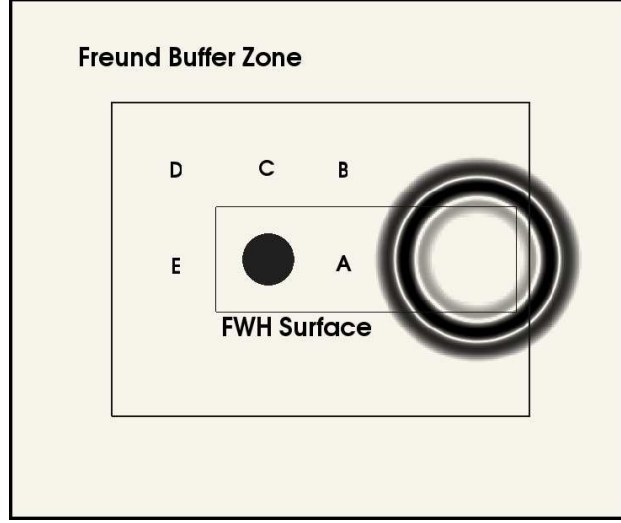


Figure 4.6: Layout of 2D acoustic scattering problem. A solid obstacle is located at the origin, and pressure waves propagate from a source centered at $(4, 0)$.

the initial conditions are a Gaussian distribution in pressure, given by the perturbation

$$p' = 10^{-3} \exp \left[-\ln(2) \left(\frac{(x-4)^2 + y^2}{0.2^2} \right) \right]. \quad (4.38)$$

The initial conditions on the native variables are then $\rho = \rho_0 + p'$, $\rho u_1 = \rho u_2 = 0$ and $e = c_p T - \frac{p}{\rho}$.

The problem is solved for $Re_a = 10^5$ on a physical domain $\Omega_P = [-3, 5] \times [-3, 3]$. The adaptive grid has 8 levels of resolution, ranging from $[16 \times 12]$ to $[2048 \times 1536]$. This resolution is not sufficient for the stability of the penalization terms at the solid interface, so artificial viscosity has been introduced. The penalization parameters are set to moderate values of $\eta_b = \eta_c = 2 \times 10^{-2}$ to reduce the size and strength of the viscous zone and to aid in a rapid calculation. The viscous zone about the obstacle has a width of $O(D10^{-2})$, where D is the cylinder diameter.

The computational domain is shown in Figure 4.6. The Freund buffer zone is clearly shown, as well as the integration surface for the Ffowcs Williams and Hawkings equation. To include all major acoustic sources, the FWH surface encompasses both the initial acoustic perturbation and the obstacle. The solution in time is examined at mid- and far-field locations A-F in Figure 4.7.

The mid-field numerical solutions (Locations A-E) correspond well with the inviscid analytical solution. Some of the error arises from the curved surfaces of the obstacle being represented

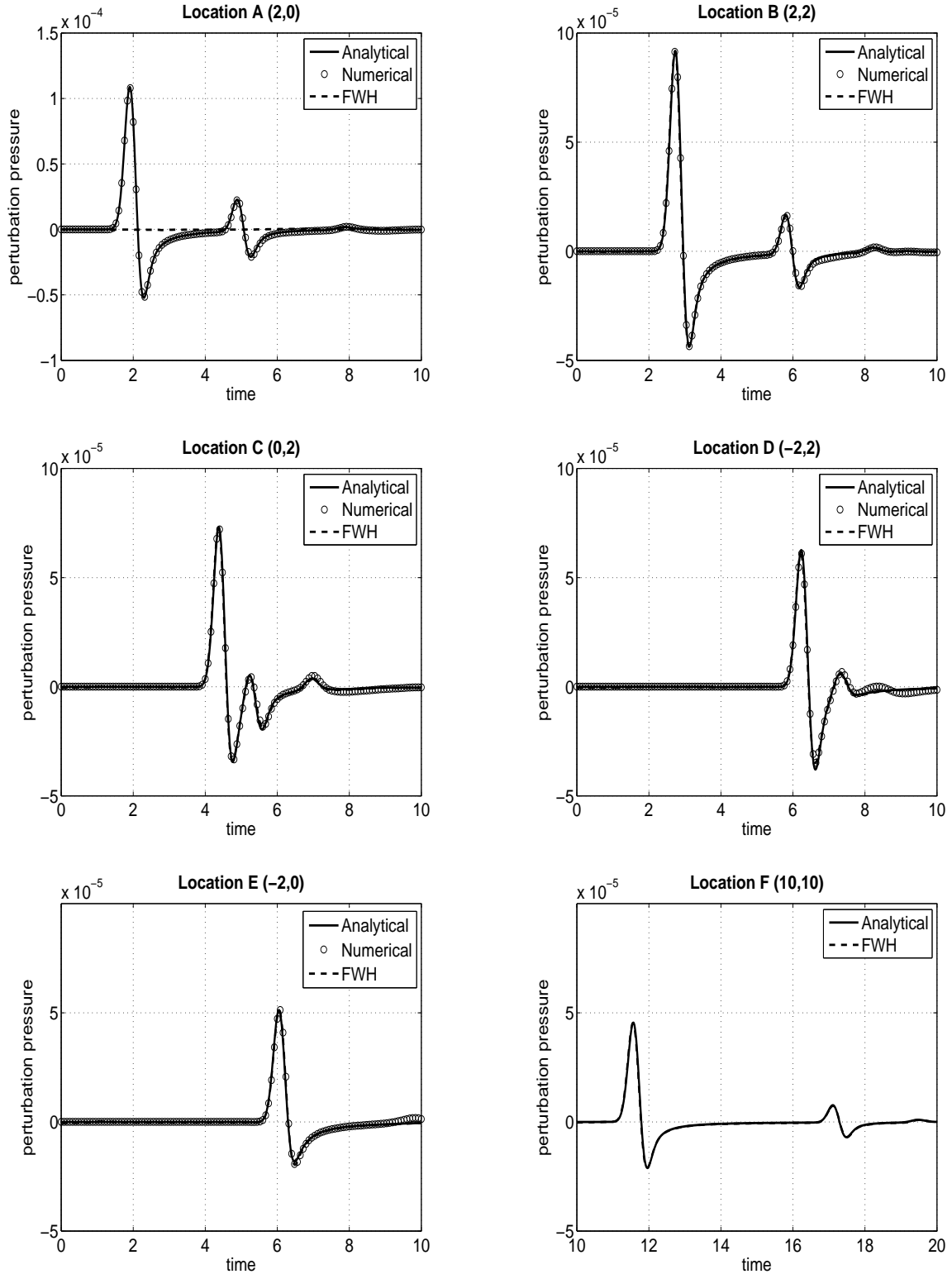


Figure 4.7: Time histories of pressure perturbations at several locations.

discretely on a rectilinear grid. Furthermore, the increased viscosity in the immediate vicinity of the obstacle dampens the wave reflection, introducing amplitude and phase errors. However, in light of the reduced computational costs, the results are quite satisfactory.

The far-field time history at Location $F = (10, 10)$ lies outside of the computational domain. The numerical solution is only determined here by the use of the FWH analogy. The advantage of this method is clearly exemplified, as an accurate solution has been obtained while limiting the computation to aeroacoustic source regions.

At many of the locations, the FWH solution is more accurate than the direct numerical calculation. This arises primarily from spurious reflections from the boundary. Location D, near the corner of the domain, is particularly prone to nonphysical reflections. Since the FWH surface is located further from the domain edge than most of the points, and does not encompass the sources of the reflections (i.e. the Freund buffer zone), these reflections have a much lower impact on the FWH solution. While a larger domain and buffer zone may be used to reduce spurious reflections in regions of interest, the use of aeroacoustic analogy obviates the need for this extra computational cost.

4.5.4 Benchmark Problem IV: Incompressible Flow Past a Circular Cylinder

In order to verify the use of artificial viscosity along the immersed boundary, incompressible flow past a circular cylinder is considered. As additional viscosity is required to stabilize the solution at more moderate resolutions, it is important to consider its effect upon the boundary layer. For low Reynolds numbers, the boundary layer behavior in the wake of a circular cylinder is well documented for both experimental and numerical cases [20, 10, 29, 8, 5]

The flow is modelled as weakly compressible with $M = 0.03$ and freestream Reynolds number of $Re = 40$ ($Re_a = 1333$). A cylinder of $r = 0.5$ ($D = 1.0$) is centered on the origin of domain $\Omega_P = [-5, 10] \times [-5, 5]$, and the penalization parameters are $\eta_b = 2 \times 10^{-2}$ and $\eta_c = 10^{-1}$. The maximum effective resolution is 2560×3840 , requiring additional viscosity to stabilize the penalization terms in the solution. The boundary layer separation point θ , and the wake length L

are both measured from the trailing edge of the cylinder.

The boundary layer separation point is highly dependent upon the Reynolds number [5]. At the resolution used, the effective freestream Reynolds number near the interface is $Re \cong 10$. From Coutanceau’s results, the corresponding separation point would be $\theta = 35^\circ$.

At steady state, the location of the boundary layer separation in this problem was found to be $\theta = 49.9^\circ$. This is markedly less than numerical results found in the literature, enumerated in Table 4.1. The artificial viscosity delays boundary layer separation. For problems that are highly sensitive to separation locations, the use of artificial viscosity ought to be minimized by the use of high resolutions.

Even with this discrepancy, the wake length and drag coefficient agree well with previously established results. The symmetrical separation region is $L = 2.22$, and the drag coefficient is $C_D = 1.52$. Compare this with the results in Table 4.1.

	Θ	L	C_D
Dennis and Chang [8]	53.8°	2.35	1.52
Fornberg [10]	55.6°	2.24	1.50
Tullio et al. [7]	53.7°	2.23	1.49
Present	49.9°	2.22	1.52

Table 4.1: Numerical results for incompressible flow past a 2D cylinder at $Re = 40$

4.5.5 Benchmark Problem V: Vortex Shedding from a Circular Cylinder

This problem considers impulsively started flow of $M = 0.2$ and $Re_a = 750$ ($Re = 150$) on the physical domain $\Omega_P = [-5, 10] \times [-5, 5]$. A solid cylinder of $r = 0.5$ is located at the origin. For CBVP, penalization parameters of $\eta_b = 2 \times 10^{-2}$ and $\eta_c = 10^{-1}$ are used. The maximum effective resolution is 2560×3840 , requiring a viscous zone with effective Reynolds number $Re \cong 10$ along the solid interface.

Since the physical domain does not fully encompass the wake, strong vortices are convected out of the x max boundary. Therefore, quadrupole sources are lost from the aeroacoustic solution.

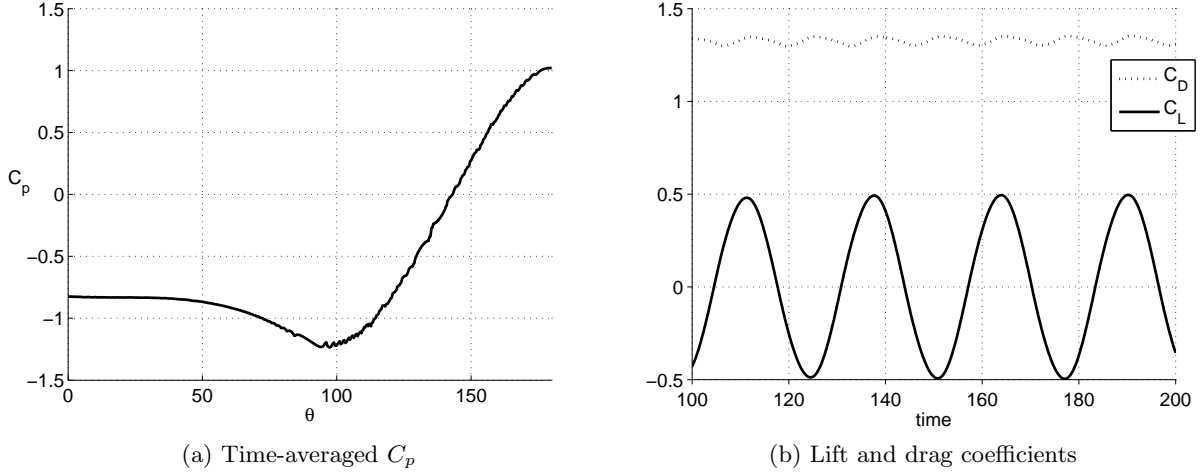


Figure 4.8: Force coefficients at $Re = 150$

However, the dipole sources arising from unsteady surface pressures dominate the solution at such a low Reynolds number [23]. For integration of the FWH equation in the frequency domain, a combined Hanning/Dirichlet windowing function is used, with the Dirichlet function covering 75% of the signal sample.

The time-averaged pressure coefficient, C_p , is shown in Figure 4.8a, normalized to the leading edge stagnation point. Note that $\theta = 0^\circ$ corresponds with the trailing edge of the cylinder. The noise is an artifact of the representation of a circle on a rectilinear grid and the interpolation of surface points. Time variant force coefficients are shown in Figure 4.8b. This forcing suggests perpendicular acoustic dipole sources with the lifting dipole dominant. These results correspond well with those of Inoue and Hatakeyama [16], though with a slightly lower amplitude for C_l . The Strouhal number for the shedding frequency is $St = 0.19$, which agrees well with both numerical [16] and analytical [12] results.

Cross-stream from the obstacle ($\theta = 180^\circ$), the aeroacoustic field is dominated by the shedding frequency caused by the lifting forces, shown in Figure (crosstream acoustics). Upstream from the obstacle ($\theta = 180^\circ$), the drag forces produce the next higher harmonic, though at a much lower amplitude. This directionality confirms the expected dipole radiation of sound from the cylinder.

Chapter 5

Conclusions and Future Research

5.1 Conclusions

A cohesive model has been developed here for the accurate and efficient prediction of aeroacoustic radiation on parallel processors. The use of aeroacoustic analogy and immersed boundary method allows for the use of small, structured grids, controlling the problem size.

One of the principle outcomes is the development of a new penalization method for immersed boundaries where individual conditions can be imposed naturally. For viscous flow and acoustic propagation, this method has shown to be accurate with a rigorously controllable error. The results on a series of benchmark problems agree well with previously established results, validating the method on the acoustic timescale. Owing to the general nature of the immersed boundary conditions, this volume penalization method can be applied beyond fluid dynamics to a wide variety of physical models.

One of the principle difficulties is the CFL limit that is imposed by the convective penalization term, η_c . For small η_c , instabilities result for problems solved on the acoustic timescale using Krylov-space time integration. This is mitigated through the use of upwind-differencing in penalized regions, as well as the greater error introduced by η_b terms.

5.2 Future Research

While the ability to use CAD generated geometry to define penalization masking functions is a powerful asset for Brinkman penalization, it is insufficient for the volume penalization method.

Since CVPM also requires distance functions and surface normals, extension of IGES file analysis would be a worthwhile platform for further development.

Characteristic-based volume penalization can also be extended into problems of higher complexity, including supersonic and three-dimensional domains and problems with moving obstacles. Such cases would provide a comprehensive foundation for the use of CBVP with the Navier-Stokes equations.

Additionally, CBVP has only been used here for low Reynolds number viscous flows, where the Navier-Stokes equations can be solved directly. Many aeroacoustic flows of interest occur at high Reynolds numbers, requiring turbulence modelling. Further work can be done to apply CBVP to turbulence equations, including Reynolds-Averaged Navier-Stokes (RANS) and Large Eddy Simulation (LES).

One of the advantages to CBVP is the ability to implement general Neumann boundary conditions. The use of this method on problems involving heat transfer at a solid interface are yet unexplored.

Lastly, the CFL limit imposed by the η_c convective term can become problematic. Circumventing this problem using alternative time integration methods, or a split time step is worth further investigation for developing the practical usefulness of CBVP.

Bibliography

- [1] P. Angot, C.-H. Bruneau, and P. Fabrie. A penalization method to take into account obstacles in viscous flows. Numerische Mathematik, 81:497–520, 1999.
- [2] Youngmin Bae and Young J. Moon. On the use of brinkman penalization method for computation of acoustic scattering from complex boundaries. Computers & Fluids, 55(0):48–56, 2012.
- [3] H.C. Brinkman. On the permeability of media consisting of closely packed porous particles. Applied Scientific Research, 1(1):81–86, 1947.
- [4] John Rozier Cannon. The One-Dimensional Heat Equation. Addison-Wesley, 1984.
- [5] M. Coutanceau and R. Bouard. Experimental determination of the main features of viscous flow in the wake of a circular cylinder in uniform translation. part 1. steady flow. Journal of Fluid Mechanics, 79:231–256, 1977.
- [6] H.P.G. Darcy. Les fontaines publiques de la ville de dijon. Victor Dalmont, Paris, 1856.
- [7] M.D. de Tullio, P. De Palma, G. Iaccarino, G. Pascazio, and M. Napolitano. An immersed boundary method for compressible flows using local grid refinement. Journal of Computational Physics, 225:2098–2117, 2007.
- [8] S.C.R. Dennis and Gau-Zu Chang. Numerical solutions for steady flow past a circular cylinder at reynolds numbers up to 100. Journal of Fluid Mechanics, 42:471–489, 1970.
- [9] D.L Donoho. Interpolating wavelet transforms. Technical Report 408, Department of Statistics, Stanford University, 1992.
- [10] Bengt Fornberg. A numerical study of steady viscous flow past a circular cylinder. Journal of Fluid Mechanics, 98:819–855, 1980.
- [11] J.B. Freund. Proposed inflow/outflow boundary condition for direct computation of aerodynamic sound. AIAA Journal, 35(4):740–742, 1997.
- [12] J. H. Gerrard. Measurements of the sound from circular cylinders in an air stream. Proceedings of the Physical Society, 68(7):453–461, 1955.
- [13] R. Ghias, R. Mittal, and H. Dong. A sharp interface immersed boundary method for compressible viscous flows. Journal of Computational Physics, 225:528–553, 2007.

- [14] S. Ghosh. On a fundamental physical principle underlying the point location algorithm in computer graphics. IEEE Transactions on Education, 42:200–204, 1999.
- [15] M.E. Goldstein. Aeroacoustics. McGraw-Hill, Inc., 1979.
- [16] O. Inoue and N. Hatakeyama. Sound generation by a two-dimensional circular cylinder in a uniform flow. Journal of Fluid Mechanics, 471:285–314, 2002.
- [17] N.K.-R. Kevlahan and O.V. Vasilyev. An adaptive wavelet collocation method for fluid-structure interaction. SIAM Journal on Scientific Computing, 6(26):1894–1915, 2005.
- [18] M.J. Lighthill. On sound generated aerodynamically. i. general theory. Proceedings of the Royal Society of London. Series A. Mathematical and Physical Sciences, 211(1107):564–587, 1952.
- [19] M.J. Lighthill. Waves in Fluids. Cambridge University Press, 1978.
- [20] Mark N. Linnick and Hermann F. Fasel. A high-order immersed interface method for simulating unsteady incompressible flows on irregular domains. Journal of Computational Physics, 204:157–192, 2005.
- [21] Q. Liu and O.V. Vasilyev. A brinkman penalization method for compressible flows in complex geometries. Journal of Computational Physics, 227:946–966, 2007.
- [22] Qianlong Liu. An Integrated Modeling and Simulation Approach for Flow-Generated Sound Prediction. PhD thesis, Department of Mechanical Engineering, University of Colorado, Boulder, December 2007.
- [23] D.P. Lockard. An efficient two-dimensional implementation of the fflowcs williams and hawkings equations. Journal of Sound and Vibration, 229(4):897–911, 2000.
- [24] T.J. Poinso and S.K. Lele. Boundary conditions for direct simulation of compressible viscous flows. Journal of Computational Physics, 101:104–129, 1992.
- [25] Shanon M. Reckinger. Adaptive Wavelet-Based Ocean Circulation Modeling. PhD thesis, Department of Mechanical Engineering, University of Colorado, Boulder, July 2011.
- [26] Jonathan D. Regele. Numerical Modeling of Acoustic Timescale Detonation Initiation Using the Adaptive Wavelet-Collocation Method. PhD thesis, Department of Mechanical Engineering, University of Colorado, Boulder, February 2008.
- [27] P.J. Schneide and D.H. Eberly. Geometric Tools for Computer Graphics. Morgan Kaufmann Publishers, San Francisco, CA, 1st edition, 2003.
- [28] K.W. Thompson. Time dependent boundary conditions for hyperbolic systems. Journal of Computational Physics, 68(1):1–24, 1987.
- [29] D.J. Tritton. Experiments on the flow past a circular cylinder at low reynolds numbers. Journal of Fluid Mechanics, 6:547–567, 1959.
- [30] US Product Data Association. Initial Graphics Exchange Specification IGES 5.3, 1996.

- [31] K. Vafai and C.L. Tien. Boundary and inertia effects on flow and heat transfer in porous media. International Journal of Heat and Mass Transfer, 24:195–203, 1981.
- [32] O.V. Vasilyev. Solving multi-dimensional evolution problems with localized structures using second generation wavelets. International Journal of Computational Fluid Dynamics, Special issue on High-resolution methods in Computational Fluid Dynamics, 17(2):151–168, 2003.
- [33] O.V. Vasilyev. Solving multi-dimensional evolution problems with localized structures using second generation wavelets. International Journal of Computational Fluid Dynamics, 17:151–168, 2003.
- [34] O.V. Vasilyev and C. Bowman. Second generation wavelet collocation method for the solution of partial differential equations. Journal of Computational Physics, 165:660–693, 2000.
- [35] O.V. Vasilyev and S. Paolucci. A dynamically adaptive multilevel wavelet collocation method for solving partial differential equations in a finite domain. Journal of Computational Physics, 125:498–512, 1996.
- [36] O.V. Vasilyev, Yu. Yu. Podladchikov, and D.A. Yuen. Modeling of viscoelastic plume-lithosphere interaction using adaptive multilevel wavelet collocation method. Geophysics Journal International, 3(147):579–589, 2001.
- [37] M. Wang, J.B. Freund, and S.K. Lele. Computational prediction of flow-generated sound. Annual Review of Fluid Mechanics, 38:438–512, 2006.